



# Improvement of spatial-temporal urban heat island study based on local climate zone framework: A case study of Hangzhou, China



Shi Yin <sup>a,b</sup>, Songyi Xiao <sup>a</sup>, Xiaotian Ding <sup>c</sup>, Yifan Fan <sup>c,d,e,\*</sup>

<sup>a</sup> Institute of Energy and Power Engineering, College of Mechanical Engineering, Zhejiang University of Technology, Hangzhou, 310023, China

<sup>b</sup> State Key Laboratory of Green Building, Xi'an University of Architecture and Technology, Xi'an, 710055, China

<sup>c</sup> Department of Architecture, College of Civil Engineering and Architecture, Zhejiang University, Hangzhou, 310058, China

<sup>d</sup> Center for Balance Architecture, Zhejiang University, Hangzhou, 310058, China

<sup>e</sup> International Research Center for Green Building and Low-Carbon City, International Campus, Zhejiang University, Haining, 314400, China

## ARTICLE INFO

### Keywords:

Urban heat island  
Local climate zone  
Urban weather generator  
Multiscale study  
Spatiotemporal analysis

## ABSTRACT

Large-scale long-period urban heat island (UHI) intensity (UHII) prediction with high spatiotemporal resolutions, satisfactory accuracy, and calculation efficiency is crucial and challenging for UHI mitigation studies. This study proposes a framework combining an urban weather generator (UWG), local climate zone (LCZ), deep-learning method, and Python automatic cyclical calculation to obtain hourly UHII throughout one year and over a total of 1920 blocks in Hangzhou City. The spatial-averaged hourly UHII are between  $-2^{\circ}\text{C}$  and  $6^{\circ}\text{C}$  in more than 96 % time, and those at  $0^{\circ}\text{C}$ – $1^{\circ}\text{C}$  contribute to 43.80 % of the total time. Spring gives the most intense nocturnal UHII, while winter has the weakest one. A significant diurnal UCI phenomenon could accompany the strong nocturnal UHI phenomenon. From the synthetic (based on seasonal data) 24-h curves, mean UHII and UCII (average of the positive and negative values, respectively) drop by approximately 25 % in winter compared to spring. Spatially, UHII is higher in the central regions with compact buildings but significantly lower in the high-vegetation-coverage regions. Based on LCZ framework, LCZ 1 (compact high-rise configurations) has the highest UHII, independent of examined periods. UHII relations to building coverage, vegetation ratio, and building height are individually quantified. The building coverage has the highest influence on annual UHII, with a correlation coefficient as high as 0.76. Results indicate that, for UHI mitigation purposes, the percentage of compact high-rise configurations (LCZ 1) in the urban area shall be limited, and the vegetation ratio is better to be greater than 20 %.

## 1. Introduction

The proportion of the world population in urban areas was 55 % in 2018 and is expected to increase to 68 % by 2050. The urban population proportion of China will increase to 80 % by 2050 [1]. Rapid urbanization changes and affects the urban climate environment significantly [2–4]. One prominent environmental impact is the urban heat island (UHI) effect, referring to the hotter urban climate than rural one [5]. UHI is drawing increasing attention because it affects resident health and building energy consumption [6,7], especially under the background of global warming and heat wave episodes [8–10].

UHI exhibits complex intra-urban spatial-temporal variations, closely related to urban underlying surfaces [11–17]. Detailed local UHI studies are crucial for revealing UHI mitigation/adaption mechanisms

and accurately modeling building energy consumption [18–21]. Studies have been dedicated to quantifying the influence of underlying surface parameters on UHII (e.g. Ref. [11]). A critical urban surface classification used in local UHI research [22–25] is the local climate zone (LCZ) framework proposed by Stewart and Oke [26]. The typical urban information used to establish LCZ classification is the building coverage, building height, anthropogenic heat, permeability, and thermal properties of underlying surfaces. LCZ method is a clear standard and has extensive adaptability in urban climate mapping [27–33]. For example, Rodler and Leduc [34] have conducted a study to obtain a fine-grain formalism of LCZ classification based on standard geographical information of the city. The high correlation between UHI intensity (UHII) and LCZ type is well-documented [35–39]. Usually, the built LCZs exhibit greater temperatures than land-covered LCZs [35,36,40].

\* Corresponding author. Department of Architecture, College of Civil Engineering and Architecture, Zhejiang University, Hangzhou, 310058, China.

E-mail address: [yifanfan@zju.edu.cn](mailto:yifanfan@zju.edu.cn) (Y. Fan).

Accurate urban air temperature data are essential to study UHI but is challenging because of the extreme complexity of the urban climate. Some studies obtained the air temperature from limited weather stations and mobile monitoring [41–43]. For example, Chen et al. [32] employed mobile measurements and Geographic Information System (GIS)-based method to develop a stepwise multiple regression model for predicting UHII spatial distribution within the primary urban area of Changsha. Nikolai et al. [44] investigated the hourly UHI variations, heat index, and thermal discomfort in Manaus (Brazil) based on temperature and air humidity from six meteorological stations. Zou et al. [45] obtained high-spatial-resolution thermal data by performing a moving transect experiment with an electric bicycle at 2-h intervals. They investigated the interaction between UHI effects and heat waves under different land use/cover types in Shenzhen, China. Although it can get real-time temperature data, the field measurement is usually challenging to cover a wide-range area and long duration with high spatiotemporal resolution simultaneously, limited by its expansive financial and human resource costs.

Due to the development of computer technology, UHI simulation is attracting increasing attention. Computational fluid dynamics can accurately simulate urban microclimate at building and neighborhood scales and explore the coupling effect of urban climate and building energy consumption [46,47]. However, the computational load is massive, restricting its application in larger-scale investigations. The weather research and forecasting model (WRF) has been widely used in simulating UHI and its mitigation strategies [48–50]. It can simulate urban climate on city- and regional-scales [27,51]. However, the computational efficiency of WRF is low, spatiotemporal resolution is limited, and simulation accuracy is moderate.

Urban weather generation (UWG), proposed by Bueno et al. [52], can be used for calculating urban canopy air temperature based on rural weather data and city morphological information [53,54]. Due to the computational efficiency of the models, UWG simulation can effectively obtain hourly UHII over long periods (e.g., years). Studies have employed UWG to analyze UHII of some typical urban samples [55–59]. Particularly, UWG and LCZ combination has been well-documented for UHI analysis. Martinez et al. [54] adopted LCZ-UWG combined framework to characterize the neighborhood-scale microclimate using two indicators: UHI and overheating intensity. Boccalatte et al. [59] employed UWG models to calculate UHI maps for 10 microclimate zones. By combining LCZ and UWG, Zhang et al. [40] selected one representative block in each LCZ to simulate the block-scale urban canopy UHI effect in Beijing. Liu et al. [22] investigated UHI phenomenon under various regional climate conditions and urban morphologies, highlighting that building density might play a more fundamental role in UHI mitigation than building height, especially for cities with weak winds. Sensitivity studies have been conducted to investigate the importance of UWG input parameters to UHII. Salvati et al. [60] maintained that urban morphology is the most critical input variable of UWG on the annual average UHII. Similarly, Litardo et al. [56] proposed that the building coverage, facade-to-site ratio, and traffic variables are more crucial to UHII than others. Based on 10 typical LCZs in Guangzhou city, Xu et al. [12] evaluated the planning strategies for UHII. They maintained that the building height and density influence UHII the most. Xu et al. [55] also presented significant improvements and extensions to UWG. Novel enhancements include the integration of advanced algorithms for simulating atmospheric boundary layer processes, contributing to more accurate microclimate modeling. The existing studies have justified that UWG has considerable potential to be applied for UHI studies in large areas (e.g., city-scale) with high spatiotemporal (500 m and 1 h) resolution and long periods (yearly or decades) attained.

However, limited studies exist about the wide-range UHI map with high spatiotemporal resolutions, particularly about efficiently resolving over a city-scale urban area throughout the whole year. Additionally, research on LCZ-based UHI features under multiple timescales is limited. Therefore, this study aims to (1) establish a framework for large-scale

(city-scale), long-period, and high-spatial-resolution (500 m) UHI modeling using the entire primary area of Hangzhou City as an example, (2) apply the framework to generate UHI maps at multiple timescales to endorse fundamental urban areas in urgent UHI mitigation needs, especially under the background of global warming and extreme heat waves, and (3) quantify the relationship between UHII and the characteristics of underlying surfaces at varied time scales. Previous sensitivity studies [56,60] have stated the importance of urban morphology on UHII. Then, the aim (3) will also focus on verifying the relationship between UHII and typical input parameters of UWG model to develop future strategies for UHI alleviation.

The paper is organized as follows. Section 2 introduces framework of UHII simulation for the entire primary area of Hangzhou City. The results are analyzed in Sections 3. Specifically, Section 3 presents spatio-temporal UHI features at multiple timescales, covering annual to hourly analysis. Section 3 also explores the underlying surface influence on UHII based on LCZ framework. Section 4 discusses practical guidance/recommendations, limitations, and future work. Finally, conclusions are drawn in Section 5.

## 2. Methodologies

### 2.1. Study area and climate description

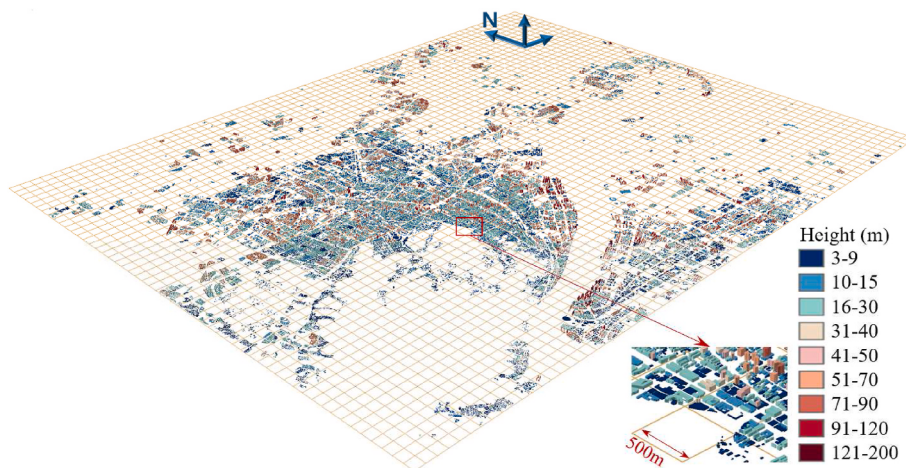
UHI analysis is based on Hangzhou City ( $29^{\circ}11' \text{--} 30^{\circ}33' \text{ N}$ ,  $118^{\circ}21' \text{--} 120^{\circ}30' \text{ E}$ ) of Zhejiang Province in southeastern China. Hangzhou has 12.20 million population and 1.81 trillion (in Chinese Yuan) gross domestic product in 2021. It is characterized as a Cfa (C: warm temperate climate, f: fully humid, a: hot summer) climate type, according to the Köppen–Geiger climate classification [61]. The city experiences distinct seasons, with hot, humid summers and cold, dry winters. Meteorological data spanning from 2015 to 2019 reveal following seasonal patterns. The average air temperature in summer (June–August) is  $27.67^{\circ}\text{C}$ . July is the hottest month, with an average temperature of  $29.10^{\circ}\text{C}$ . The mean value of the daily highest hourly temperatures in July can reach  $37.12^{\circ}\text{C}$ , and extreme high temperatures could be up to  $40.50^{\circ}\text{C}$ . The average temperature in winter (December–February) is  $6.35^{\circ}\text{C}$ . January is the coldest month, with an average temperature of  $5.17^{\circ}\text{C}$ . The mean value of the daily lowest hourly temperatures in January is  $0.64^{\circ}\text{C}$ . Spring (March–May) and autumn (September–November) experience similar temperatures, with an average of  $17.21^{\circ}\text{C}$  and  $18.71^{\circ}\text{C}$ , respectively.

Fig. 1 shows the building map of Hangzhou City generated by ArcGIS, with the original data from Baidu Maps (<https://map.baidu.com/>). Most buildings are 15 m–40 m high. The different underlying surface characteristics can generate distinct thermal environments. For a detailed high-spatial-resolution investigation, the targeted constructed area ( $901 \text{ km}^2$ ) is divided into multiple  $500 \times 500 \text{ m}^2$  blocks for the neighborhood-scale UHI study (Fig. 1) [30,62]. Finally, 3604 blocks are generated, with 1920 blocks containing buildings. Because UWG simulations need building information (e.g., building coverage and mean building height), these 1920 blocks qualify for subsequent UWG simulation. UWG simulates the canopy air temperature in each qualified block. Finally, a high-spatial-resolution UHII map of Hangzhou City could be available. Detailed simulation methods are introduced in Sections 2.2 and 2.3.

### 2.2. UHI simulation strategy in this study

The principal strategy for the UHI study is to use UWG for estimating hourly urban canopy air temperature [59]. The basic flow chart is plotted in Fig. 2, with main steps described in detail as follows.

The urban morphological information and rural weather files are the primary inputs to UWG [55,63]. The input urban morphological information includes the climate zone (3A for Hangzhou [64]), vegetation details (including tree and grass coverage), building features (including



**Fig. 1.** Map of the study area and its block division using  $500\text{ m} \times 500\text{ m}$  grids.

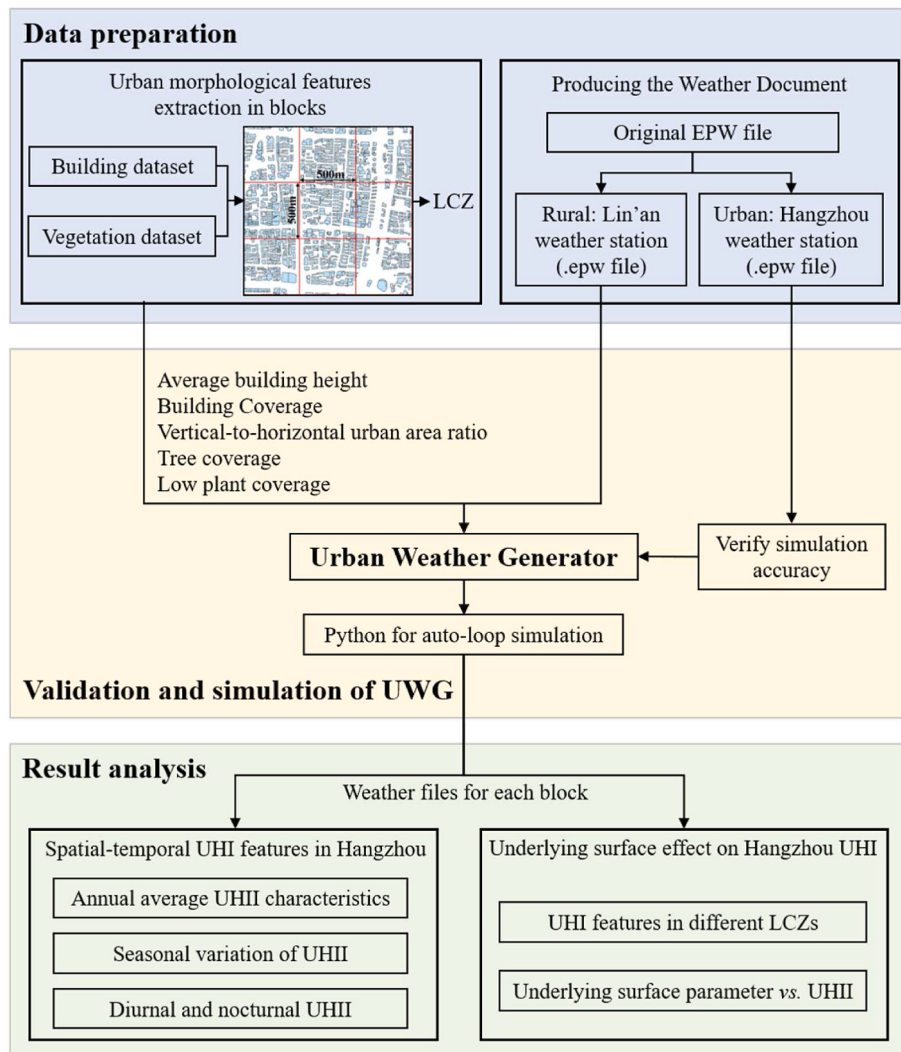


**Fig. 2.** Workflow of urban heat island (UHI) simulation in Hangzhou City.

building type, building waste heat emissions from air-conditioning systems, facade glass ratio, mean building height, building coverage, and facade-to-site ratio), and urban canyon characteristics (including geometry and heat transfer properties, e.g., albedo, emissivity, thermal

conductivity, and volumetric heat capacity).

In this study, the mean building height, building coverage, facade-to-site ratio, and vegetation coverage vary in different blocks. Related data acquisition is introduced in Section 2.3.2. For other parameters, the

default values in UWG models are adopted and kept constant for all blocks ([Table 1](#)).

The rural weather data are imported into UWG in an EnergyPlus Weather (EPW) file format. The weather data in EPW file include outdoor air temperature, wind speed and direction, beam and diffuse radiation, relative humidity, and atmospheric pressure. It also includes geographic location information (latitude and longitude) for the rural weather station. Moreover, a statistics report of the annual weather data (STAT file) is used to determine ASHRAE climate zone to which the city belongs. The detailed acquisition of weather data will be introduced in Section [2.3.1](#).

Once the input is completed, resolving the urban air temperature by UWG depends on four coupled physical models: rural station model (RSM), vertical dispersion model (VDM), urban boundary layer (UBL) model, and urban canyon-building energy model (UC-BEM) [65]. RSM reads the hourly air temperature and velocity measured at the rural weather station, calculates the rural sensible heat flux, and provides it to VDM and UBL models ([Fig. 3](#)). VDM calculates a vertical air temperature profile above the rural weather station, provided to UBL model. UBL model calculates the air temperature above the urban canopy based on the output from VDM and RSM and the urban sensible heat fluxes from UC-BEM. Finally, the air temperature in urban canyons can be obtained in UC-BEM.

This study conducts UWG simulation through a Python program as a plug-in integrated into Grasshopper. A Python auto-loop program was particularly developed to invoke UWG package for automatic cyclical simulation over all built-up blocks (total 1920 blocks) in Hangzhou City. Hourly temperatures throughout the year are obtained for each  $500 \times 500 \text{ m}^2$  blocks (total 1920 blocks). It facilitates UWG application over the whole city. Therefore, UHII mapping can be achieved over a large spatial scale (city-scale). The abovementioned UHI simulation can be finalized within seven days by implementing on an ordinary desktop (Intel® Core™ i7-10700 CPU, 2.90 GHz, RAM 24.0 GB). The spatio-temporal UHI features at multiple time scales (annual, seasonal, and 24-h daily scales), and the urban morphology influence on UHII can be analyzed.

Validating UWG models is challenging because the magnitude of UHI effect depends on the choice of weather station. This study partially validates UWG simulation based on Hangzhou urban weather station measurements. The measured air temperatures are compared with the simulated ones from UWG. Detailed validation work is introduced in Section [2.4](#).

### 2.3. Data acquisition

For a high-spatial-resolution UHI study, the targeted constructed area of Hangzhou City is divided into multiple  $500 \times 500 \text{ m}^2$  blocks ([Fig. 1](#)). The climatic and morphological data required for UWG input are collected in each block. [Fig. 4](#) is a workflow diagram of data

**Table 1**

Primary input properties of the urban surface for urban weather generator (UWG) model.

Parameter	Value
Wall R-value	$0.61 \text{ m}^2 \text{ K/W}$
Roof R-value	$2.44 \text{ m}^2 \text{ K/W}$
Window U-factor	$4.09 \text{ W}/(\text{m}^2 \cdot \text{K})$
Solar heat gain coefficient (SHGC)	0.25
Road albedo	0.10
Road pavement thickness	0.50 m
Road pavement conductivity	$1 \text{ W}/(\text{m} \cdot \text{K})$
Vegetation albedo	0.25
Non-building sensible heat at street level	$20 \text{ W}/\text{m}^2$
Building type	Large office (40 %); Apartment (60 %)
Mean building height, building coverage, facade-to-site ratio, vegetation coverage	See Section <a href="#">2.3.2</a> for details.

acquisition and preparation. Details will be introduced in Sections [2.3.1](#) (for climatic data) and [2.3.2](#) (for urban morphological data).

#### 2.3.1. Climatic data

In this study, five weather station candidates are available after considering the climate data quality: two urban (Hangzhou and Xiaoshan stations) and three rural stations (Tonglu, Lin'an, and Jiande stations). The Hangzhou station is chosen for the urban weather station because it locates in the center of the primary urban area and can well represent the urban climates. Tonglu and Jiande stations are further from Hangzhou station, with many mountains and rivers between them and Hangzhou, while Lin'an station is the closest one to the urban station. Therefore, Lin'an station is selected as the rural weather station. Additionally, from the preliminary test, Lin'an station can well represent the surrounding rural climate of Hangzhou City. It gives the smallest root mean square error (RMSE) of urban air temperature comparison when Lin'an station data are imported as the input for UWG models.

Hourly temperature data for Hangzhou and Lin'an weather stations in 2019 were obtained from the China Weather Data Network (<http://data.cma.cn/>). The hourly temperature data can be used to create two updated EPW files of rural and urban weather stations by replacing the temperature data in the original standard EPW file downloaded from the EnergyPlus website (<https://energyplus.net/>). The hourly relative humidity is not updated because it hardly changes over a long period ( $0.006 \% [10 \text{ y}]^{-1}$ ) [66]. The accessibility of hourly humidity data is also challenging. The generated rural EPW file for the Lin'an weather station (rural station) is used as UWG input in subsequent simulation. The updated temperature data for the Hangzhou weather station (urban station) are compared with the simulation results for partial UWG validation.

#### 2.3.2. Urban morphologies

This study uses Baidu Maps (<https://map.baidu.com/>) and ArcGIS software to extract individual building information. In the beginning, building footprints and the number of floors are captured. The building height is calculated by multiplying the number of floors by three. [Fig. 5](#) shows the footprints of the study area ([Fig. 5a](#)) and two examples in Qianjiang's new city's central business district (CBD) and city center ([Fig. 5b and c](#)).

The collected map data are vectorized into ESRI shape files (SHP files), which can be imported into ArcGIS for further processing. According to Hangzhou's longitude, CGC S2000 GK CM 123E is the projection coordinate system. The building perimeters and floor areas can be extracted in ArcGIS. The building facade area is calculated by multiplying the perimeter and building height.

For calculating building and vegetation coverage in each block, deep-learning identification is employed based on satellite images, as presented in previous study [67]. For the deep-learning model, a land cover classification model based on convolutional neural networks was used to automatically categorize various land cover types within satellite images. The model learns patterns and features in the training dataset through layers of artificial neurons to distinguish between classes like trees and buildings. The model is trained and validated with a land cover dataset specific to Hangzhou area, built with Gaofen2 (GF2) satellite imagery using the proposed OpenStreetMap object-based image analysis method. Finally, with a spatial resolution of  $1 \text{ m}^2$ , underlying surface types are classified into eight categories: low vegetation, trees, roads, bare lands, shadows, water, buildings, and impervious surfaces. More details about this identification method can be referred to our published work [67]. The identification results can be imported into ArcGIS as a TIF file, displaying different surface types in different colors. Then, the building and vegetation coverages of each block can be determined.

[Fig. 6](#) plots the spatial distributions of the building coverage, mean building height, and vegetation coverage. The building coverage map is characterized by a “compact center and sparse periphery” pattern. The

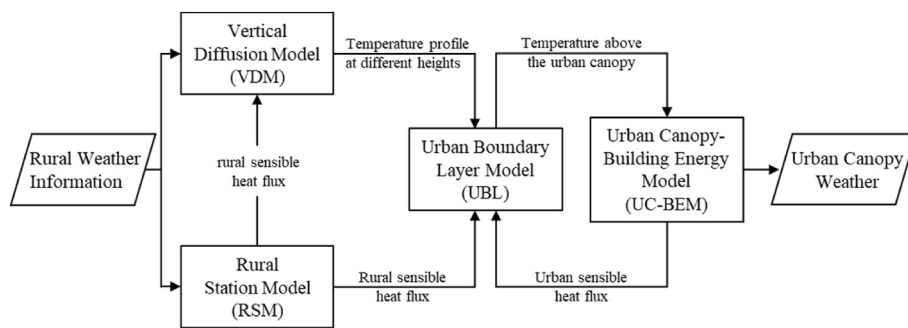


**Fig. 3.** Urban weather generator (UWG) models for resolving the urban canopy weather.

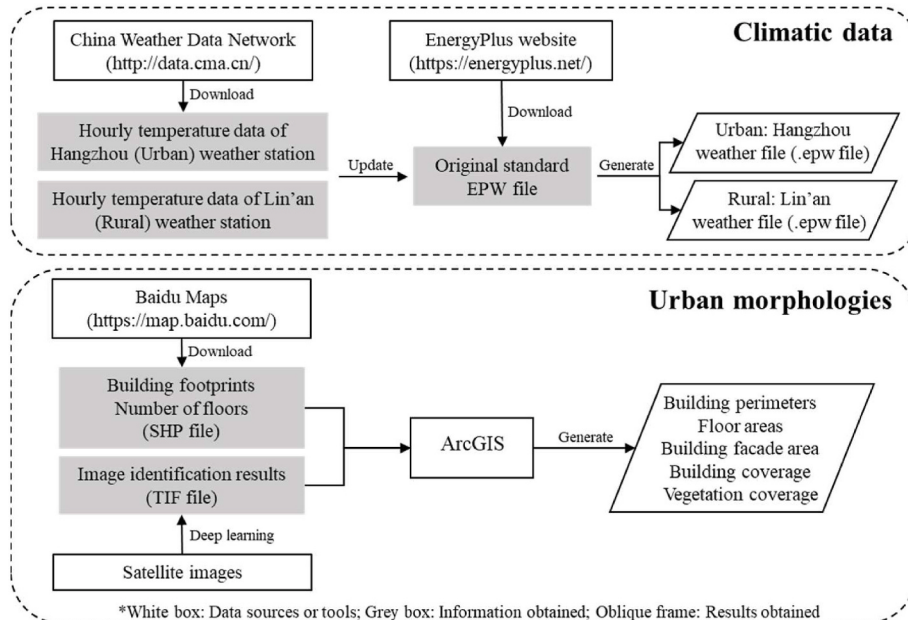


**Fig. 4.** Workflow of data acquisition and processing.

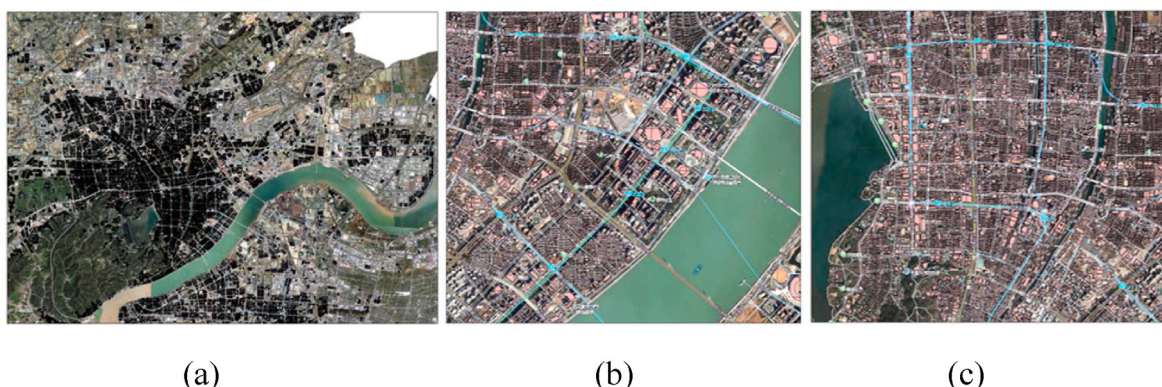


**Fig. 5.** (a) Footprints of interested urban area; (b, c) examples of building footprints in Qianjiang's new city's central business district (CBD) and city center.

compactness degree gradually weakens from the center to the surrounding regions. Most of the central area has approximately 20%–40% building coverage, accounting for 32.70 % of the total examined blocks. The building height map exhibits a discrete distribution. The high-rise buildings occupy the central area and are also common in the surrounding regions. Blocks with a mean height [20 m, 45 m] account for 29.80 % of the total blocks, whereas those in the range [0 m, 20 m]

account for 65.40 %. Unlike the building coverage distribution, the vegetation coverage is lower in the central urban areas but higher in suburban areas, particularly in the southwestern Hangzhou City. Blocks with vegetation coverage below 40 % account for 77.90 %.

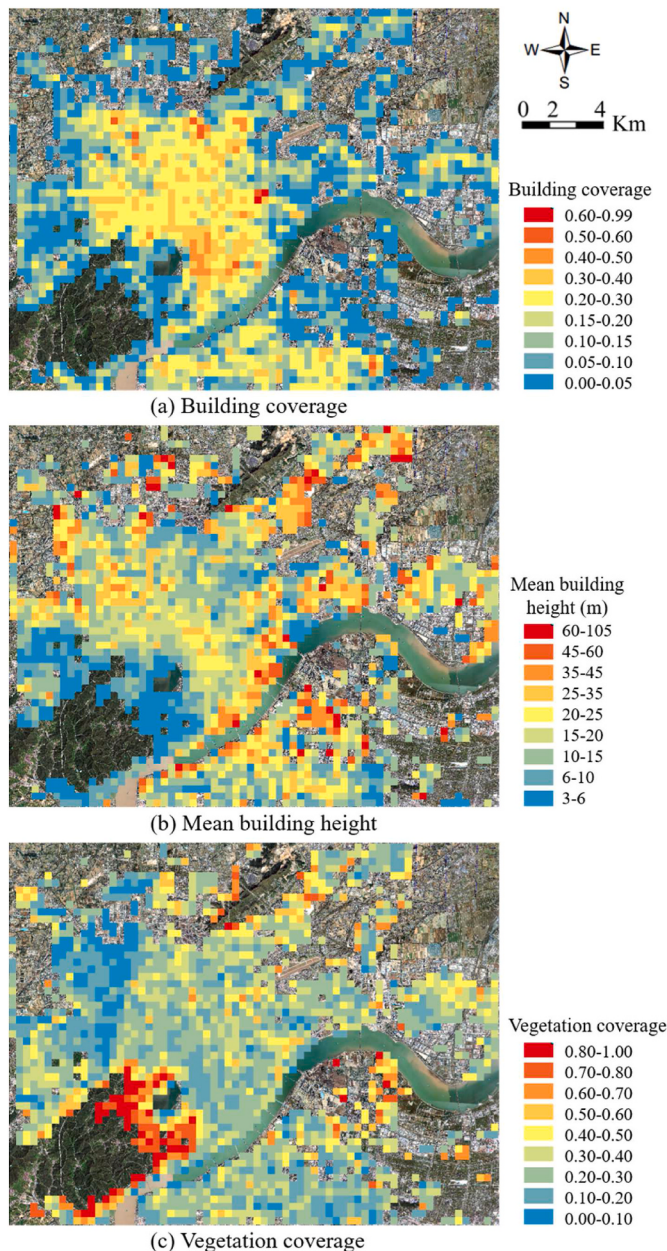


**Fig. 6.** Spatial distributions of (a) building coverage, (b) mean building height, and (c) vegetation coverage in Hangzhou City.

#### 2.4. Partial validation of UWG simulation

UWG modeling is partially validated by comparing its simulated urban air temperature with the measured data from the urban weather station. In practice, the hourly rural (Lin'an station) weather data and morphological information of Hangzhou City are imported into UWG engine for urban air temperature simulation. Then, the obtained hourly simulation results are compared with the measured urban air temperature at Hangzhou (urban) weather station, as shown in Fig. 7. Hourly deltas (simulated UHII – measured UHII) are also presented. The simulated air temperature shows a consistent and reasonable trend with the measured one at the urban weather station. The percentage of hourly delta values in  $[-2^{\circ}\text{C}, 2^{\circ}\text{C}]$  is 80.60 %.

A longer-period comparison rather than a single-day comparison is necessary to reasonably reflect the simulation accuracy and derive quantitative error estimations, due to the coupling influence of various complex factors on rural and urban air temperatures. This study further

averages air temperatures at the same hours throughout two durations, i.e., a single month and one whole year, to obtain the synthetic 24-h air temperature cycles (Fig. 8). Solid lines with symbols in Fig. 8a are the synthetic simulated hourly temperatures based on seasonal-averaged data, where  $S_1$ – $S_{12}$  indicate January–December. The corresponding hollow symbols,  $O_1$ – $O_{12}$ , represent the synthetic observed (measured) data from January–December. In Fig. 8b, the solid line represents the synthetic simulation results based on the annual data, and the squares are the observed (measured) ones. Corresponding deltas (simulated UHII – observed UHII) for the monthly and annual results are given in Fig. 8c and d, respectively.

The simulation correlates well with the measured data. Delta values all fall into the range  $[-2^{\circ}\text{C}, 2^{\circ}\text{C}]$  for the monthly comparison, with an hourly maximum absolute error of approximately  $1.76^{\circ}\text{C}$ . The comparison leads to an RMSE of  $1.06^{\circ}\text{C}$  in May and  $0.50^{\circ}\text{C}$  in January. Delta values are primarily in the range  $[-1^{\circ}\text{C}, 1^{\circ}\text{C}]$  for the annual comparison, with an hourly maximum absolute error of  $1.14^{\circ}\text{C}$ . The average RMSE is  $0.78^{\circ}\text{C}$  for monthly comparison and  $0.66^{\circ}\text{C}$  for annual comparison. The performance of UWG models was comparable to previous studies [53,59], giving a monthly RMSE of approximately  $1^{\circ}\text{C}$  [53] and an average RMSE error of  $1^{\circ}\text{C}$ – $2^{\circ}\text{C}$  for hourly temperature simulation [59]. Moreover, the annual average UHII from the simulation and measurement is  $1.12^{\circ}\text{C}$  and  $1.06^{\circ}\text{C}$ , respectively. Such simulation error is approximately 5.40 %.

In a word, our UWG simulation is reasonable and reliable. The partial UWG validation in this study can be accepted.

## 3. Results

### 3.1. Spatiotemporal UHI features in Hangzhou City

UHI exhibits highly complex spatiotemporal heterogeneity in urban areas. This study analyzes the urban canyon air temperature of 1920 blocks in Hangzhou City by automatic UWG simulation for 1 year duration with an hourly resolution. The spatiotemporal UHI characteristics are analyzed and discussed.

#### 3.1.1. Overall UHI characteristics

Typically, UHII of each block is derived by calculating the air temperature difference between urban block and reference rural weather station, i.e., subtracting rural temperature from the urban one [5,68]. Finally, the 8760-h UHII sequence can be attributed to each block. Due to the large amount of data, i.e., 1920 blocks with 8760 h data in each, for succinctness, the spatial-averaged (averaged results of 1920 blocks) hourly UHII through the year is first presented (Fig. 9), where spring, summer, autumn, and winter are March–May, June–August, September–November, and December–February, respectively.

Fig. 10 shows the frequency distribution of spatial-averaged hourly UHII using  $1^{\circ}\text{C}$  interval. The spatial-averaged hourly UHII data have a maximum value of  $13.59^{\circ}\text{C}$  and a minimum of  $-5^{\circ}\text{C}$ . In more than 96 % time (8411 h), the spatial-averaged hourly UHII are between  $-2^{\circ}\text{C}$  and  $6^{\circ}\text{C}$ . Particularly, UHII falling into  $0^{\circ}\text{C}$ – $1^{\circ}\text{C}$  contribute to 43.80 % of the total 8760 h. Some extreme hourly UHII is observed to be higher than  $10^{\circ}\text{C}$ , accounting for approximately 0.18 % of the total 8760 h. The extreme UHI induces high temperatures, threatening power grid safety, energy safety, and resident health. The extreme UHI situation should be considered carefully when designing resilient city and energy systems.

Regarding the hourly data, urban cool island (UCI) is detected due to the negative UHII values. Most urban cool island intensities (UCII) range from  $0^{\circ}\text{C}$  to  $-1^{\circ}\text{C}$ , accounting for 15.62 % of the total 8760 h. Only 3 h have the extreme UCII beyond  $-4^{\circ}\text{C}$ .

For a spatial view of UHI phenomenon, the annual average UHII in each block is given to generate the annual UHII map over a large city-scale (Fig. 11). All the studied blocks show positive values, i.e., heat islands. Some negative values (cold islands) could exist in a short timescale (hourly data in Figs. 9 and 10) but are not preserved in Fig. 11

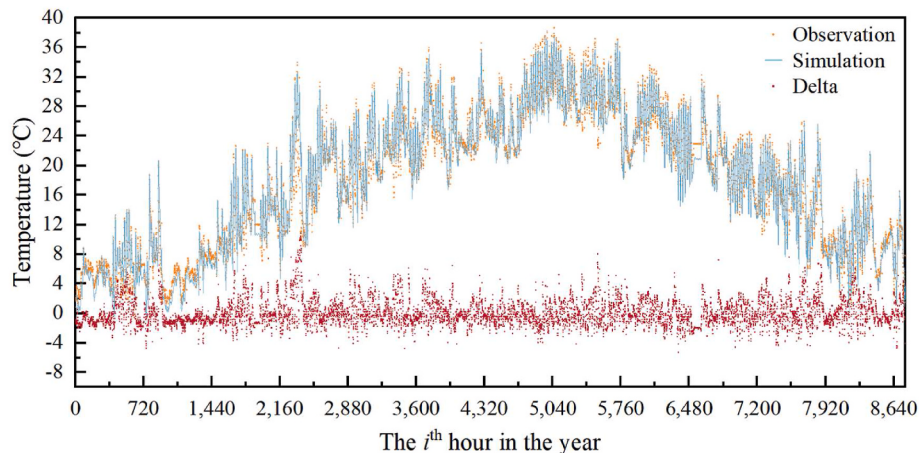


**Fig. 7.** Comparison between simulated (blue line) and measured (orange circles) annual hourly temperatures; delta (red dot) is the difference between simulated and measured UHII (simulated UHII – measured UHII). (For interpretation of the references to color in this figure legend, the reader is referred to the Web version of this article.)

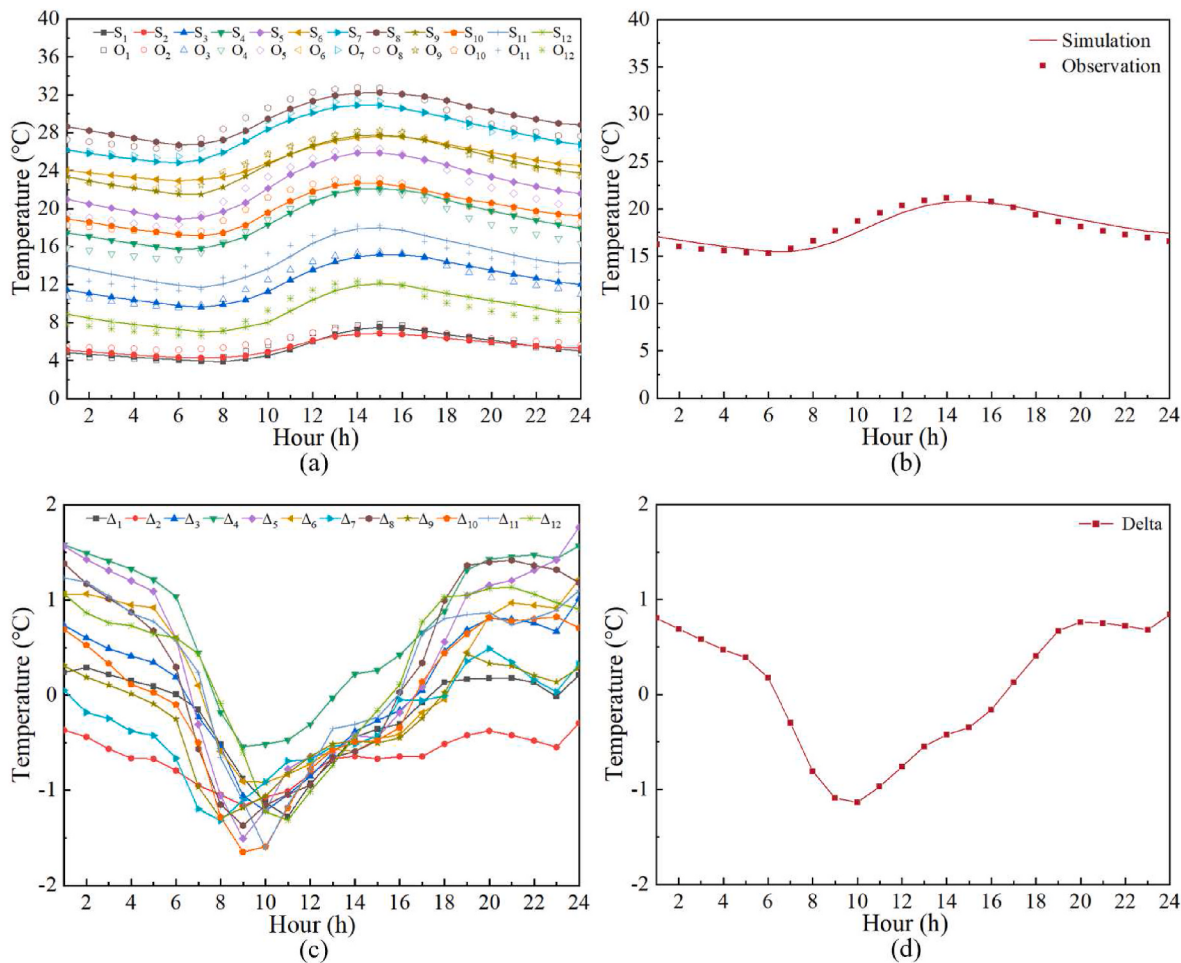


**Fig. 8.** Synthetic 24-h air temperatures based on (a) monthly and (b) annual average data, and (c–d) corresponding delta values. S: Simulation, O: Observation,  $\Delta$ : Delta values (simulated UHII – observed UHII), 1–12: January–December.

because calculating the annual average UHII neutralizes the negative values.

Based on Fig. 11, the annual average UHII is  $0.90\text{ }^{\circ}\text{C}$ – $1.90\text{ }^{\circ}\text{C}$  approximately, depending on the local underlying surface characteristics (Fig. 6). In all blocks, the minimum building cover is 0.0012 %, minimum mean building height is 3 m, and maximum vegetation

coverage is 97 %. However, these limiting values are not concurrent in one specific block.

The annual UHII distribution is influenced by the combination of building coverage, mean building height, and vegetation coverage (Fig. 6). The annual average UHII is more evident in the central and northwestern parts of the study area, where building coverage and

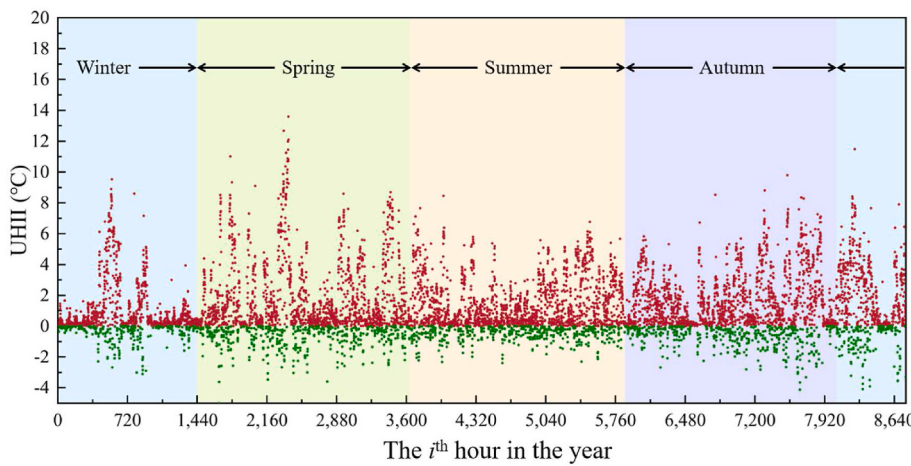


**Fig. 9.** Spatial-averaged hourly urban heat island intensity (UHII) (red/green circles: positive/negative values). (For interpretation of the references to color in this figure legend, the reader is referred to the Web version of this article.)

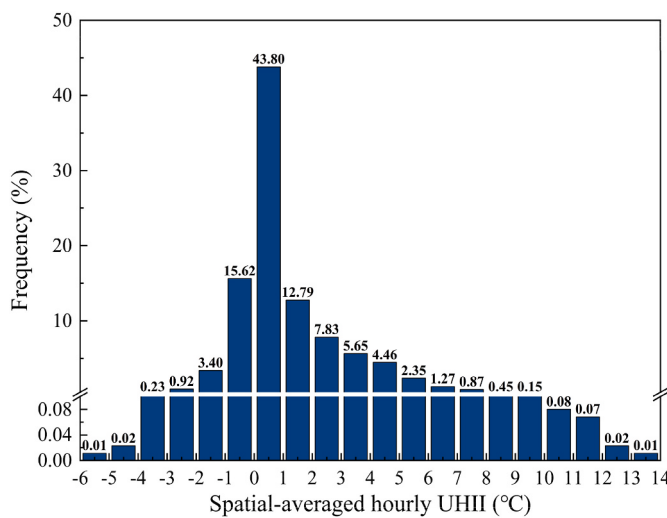


**Fig. 10.** Frequency distribution of spatial-averaged hourly urban heat island intensity (UHII).

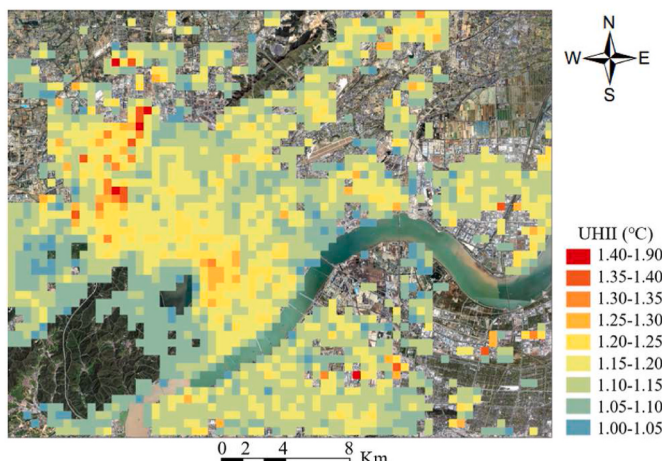


**Fig. 11.** Spatial distribution of the annual average urban heat island intensities (UHII) in Hangzhou City.

height are high, but vegetation coverage is low. The maximum annual average UHII is  $1.82^{\circ}\text{C}$  at one highly built-up block, where the building coverage is 58.57 % (a high-density area), average building height is 63 m (a high-rise building group), and vegetation coverage is 8.70 %. In the southwestern part, with high vegetation and sparse low buildings, the annual average UHII is significantly reduced. The minimum annual average UHII is  $0.97^{\circ}\text{C}$ , where the building coverage is 2.67 %, average building height is 6 m, and vegetation coverage is 71.83 %.

The hotspot identification from UHII maps would help evaluate the heat exposure of residents and locate vulnerable sites and populations more precisely. Moreover, paying attention to the UHII differences among different blocks help effectively identify heat mitigation strategies. UHII can be significantly modulated by building coverage, since the largest annual average UHII in densely built-up areas can be twice than sparsely built-up areas. The weakening effect of vegetation on UHII can be verified by UHII reduction in the northwestern part.

Based on Fig. 11, three groups of blocks are selected according to the annual average UHII, ranking the top 5 % (Group 1: UHII is  $1.23^{\circ}\text{C}$ - $1.82^{\circ}\text{C}$ ), middle 5 % (Group 2: UHII is  $1.13^{\circ}\text{C}$ - $1.14^{\circ}\text{C}$ ), and bottom 5 % (Group 3: UHII is  $0.97^{\circ}\text{C}$ - $1.05^{\circ}\text{C}$ ). In each group, smaller timescale (higher temporal resolution) UHII characteristics are investigated by analyzing daily cycles. In practice, the hourly UHII of the involved blocks in each group is averaged first, generating spatial-averaged 8760 h UHII data. Next, UHII at the same hour is further averaged, generating a synthetic 24-h UHII curve for each group (Fig. 12). Herein, the period from 8:00 to 18:00 (yellow background) is defined as daytime, and the period from 20:00 to 4:00 (green background) is defined as nighttime.

Positive UHII (UHI phenomenon) generally starts at approximately 14:00, extends to sunrise, i.e., lasting the whole night, and disappears at approximately 9:00. Such observation is consistent with previous findings [56,69]. UHII is strong at night and reaches a peak of approximately  $2.30^{\circ}\text{C}$  at 24:00. The maximum difference of hourly temperature between Groups 1 and 3 is approximately  $0.50^{\circ}\text{C}$ .

UCI phenomenon is significant during the day (Fig. 12) because the building canopy can partially block solar radiation [52]. Temperature increase in urban areas is slower and limited, while the exposed ground in the suburbs warms up faster and significantly by solar radiation [70]. Specifically, the UCI starts at approximately 9:00 and ends approximately at 14:00, with a peak magnitude of approximately  $-0.60^{\circ}\text{C}$  at 11:00, similar to previous study [56]. The UCI duration in Group 1 is slighter shorter and weaker compared with the other two groups, whereas the diurnal UCII curves are similar for Groups 2 and 3.

Variations of 24-h UHII shall be considered in building energy consumption modeling and supply-demand design, especially for

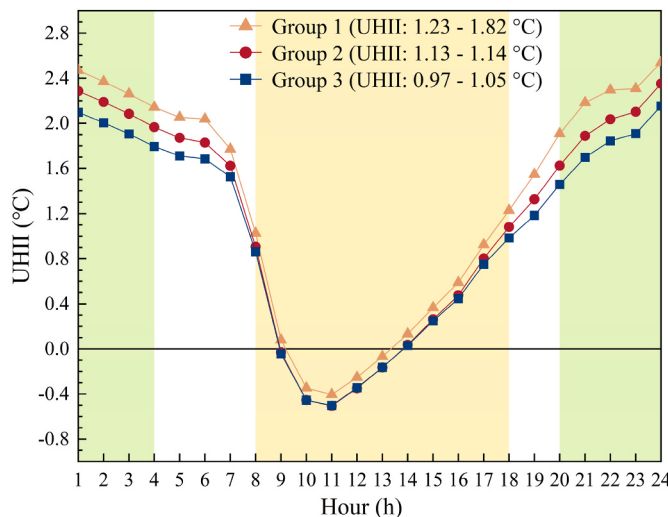


**Fig. 12.** Synthetic 24-h urban heat island intensity (UHII) curves based on annual average UHII (yellow background: daytime; green background: nighttime). (For interpretation of the references to color in this figure legend, the reader is referred to the Web version of this article.)

distributed energy systems with a large portion of renewable energy, such as the building-integrated photovoltaic (BIPV) system. Specifically, with the UHI phenomenon (positive UHII values), if rural weather data are used, cooling energy consumption will be underestimated and heating energy consumption will be overestimated. Photovoltaic (PV) system electricity modeling can be improved by UHI-induced temperature correction because air temperature can affect PV system efficiency. Finally, matching the demand-supply curve will be more precise at the design stage.

### 3.1.2. Seasonal variation of UHI

Although spatial-averaged hourly UHII in each season can be found in Fig. 9, spatiotemporal UHI characteristics of each season are exhibited in this section for a more direct and clear analysis. Fig. 13 shows seasonal-averaged UHI maps. Spatial deviation of UHII is small in a specific season, limited to approximately 0.50 °C. Still, high UHII is

observed in downtown areas. Spring gives the most intense UHII (1.20 °C–1.40 °C approximately), while winter has the weakest UHII (0.80 °C–1.00 °C approximately). By separately checking urban and rural temperatures during the day and night for different seasons, it was found that the nocturnal UHII of spring is particularly significant (more details can be referred to following Section 3.1.3), contributing to the high overall UHII in spring. Further, the strong nocturnal UHII in spring happens primarily due to lower rural air temperature. Since spring is a transition season from winter to summer, the soil thermal inertia makes the rural soil temperature low for a long time, resulting in a lower rural air temperature. The weak winter UHII might be because the winter in Hangzhou is cold (4 °C–12 °C) but without heating facilities, leading to the weakest UHII in winter.

Among all examined blocks, the spatial-averaged seasonal UHII is 1.29 °C, 1.10 °C, 1.19 °C, and 0.96 °C for spring, summer, autumn, and winter. The seasonal variation is insignificant, with a difference of approximately 0.33 °C. This may be because Hangzhou is in the warm temperate zone, with warmer seasons and abundant precipitation; therefore, the differences in temperature and precipitation between seasons are smaller. Finally, the seasonal UHII variation is less significant than other climate zones [71].

The synthetic 24-h UHII based on the seasonal temperature data is derived to investigate the seasonal heat islands at smaller timescales. In each season, UHII values of the same hours are averaged throughout the blocks and seasons. Finally, the synthetic typical 24-h UHII curves of each season are plotted (Fig. 14). Similar to the work by Litardo et al. [56], UHI and UCI phenomena (i.e., positive and negative UHII) are found in the 24-h UHII curve. The nocturnal UHI happens in all seasons, with the most evident in spring. A significant diurnal UCI phenomenon could accompany the strong nocturnal UHI phenomenon. The UHI and UCI phenomena are simultaneously weakened in winter. Particularly, in spring, the UHII has a maximum of 2.79 °C, with a mean of 1.73 °C (average of the positive values), and UCII has a negative peak of −0.63 °C, with a mean of −0.39 °C (average of the negative values). In winter, UHII achieves a positive peak of 1.83 °C, with a mean of 1.29 °C (average of the positive values), and UCII has a peak of −0.48 °C, with a mean of −0.29 °C (average of the negative values). Viewing from the synthetic (based on seasonal data) 24-h curves, mean UHII and UCII drop by approximately 25 % in winter compared to spring.

Additionally, it shall be noticed that UHII is the temperature

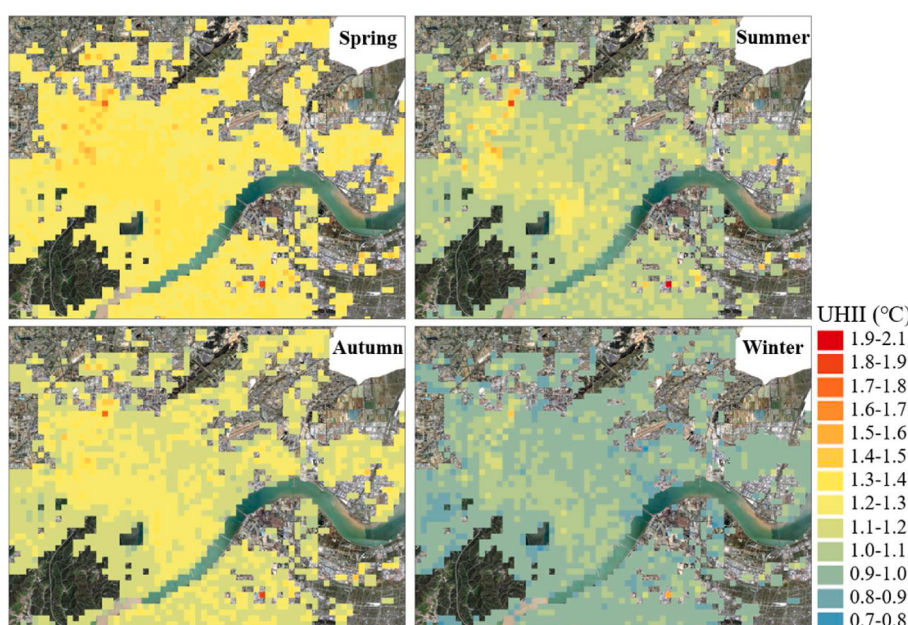


**Fig. 13.** Spatial distribution of seasonal-averaged urban heat island intensity (UHII).

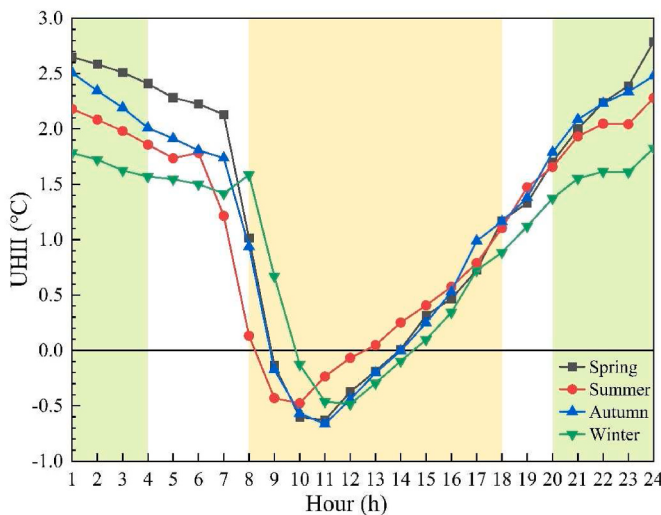


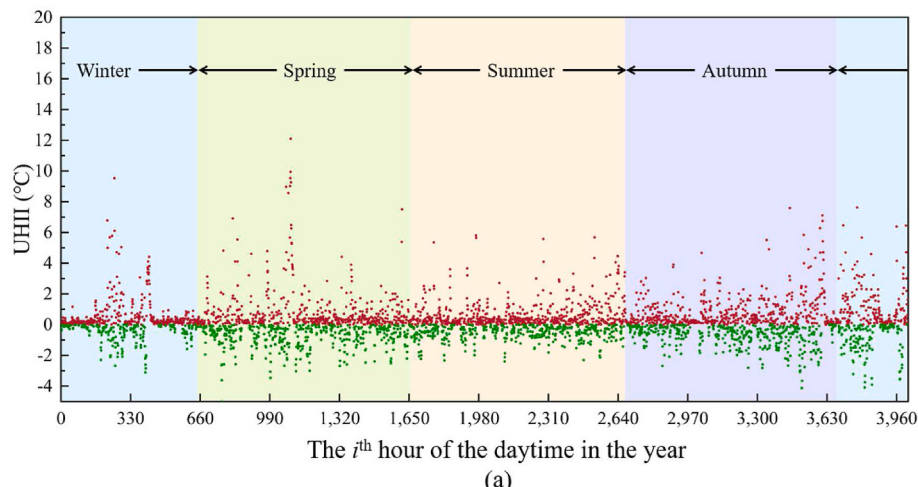
**Fig. 14.** Four synthetic 24-h urban heat island intensity (UHII) curves based on seasonal UHII data (yellow background: daytime; green background: nighttime). (For interpretation of the references to color in this figure legend, the reader is referred to the Web version of this article.)

difference between urban and surrounding rural areas, not the “absolute temperature” in the city. Therefore, a UHII reduction does not always mean the improvement of the thermal environment [72]. In our study, the summer in Hangzhou City gives weak UHI and even has UCI phenomenon during the daytime. However, it still suffers severe heat problems, and the heat mitigation demand is great.

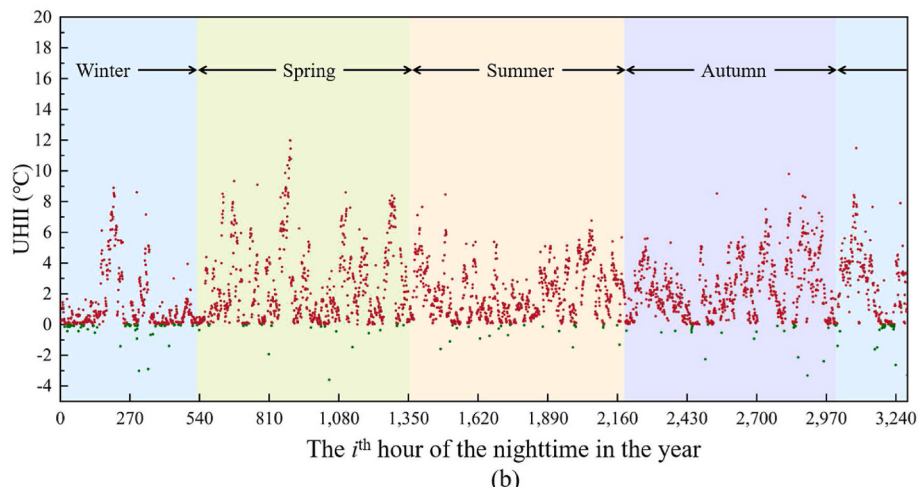
Generally, the UCI phenomenon is most pronounced around 11:00, similar to the previous study [56]. The UCI appears earlier in summer and later in winter, with a delay of approximately 1.5 h. The time of UCI peak is the same for spring and autumn, whereas it differs for summer and winter (earliest in summer), indicating that the solar altitude plays a role. The stronger solar radiation increases the rural temperature faster, reaching the largest UCI earlier. The UCI duration is approximately 4.5 h in summer and winter, with a UCI peak of  $-0.50^{\circ}\text{C}$ . In spring and autumn, the UCI curves are similar. It is preserved approximately 5 h, with a slightly stronger peak of approximately  $-0.65^{\circ}\text{C}$ . Such UHI and UCI behaviors are consistent with the energy basis in the urban area, indicating that the urban air temperature changes during the day in response to the mesoscale variations in urban and rural heating and cooling rates primarily caused by variations in radiative and thermodynamic qualities [73].

### 3.1.3. Diurnal and nocturnal UHI features

Diurnal and nocturnal UHI characteristics are crucial for evaluating the natural ventilation potential of buildings and the heat exposure of residents. In this subsection, by distinguishing daytime and nighttime



(a)



(b)

**Fig. 15.** Spatial-averaged hourly urban heat island intensities (UHII) in (a) the daytime and (b) nighttime (red/green circles: positive/negative). (For interpretation of the references to color in this figure legend, the reader is referred to the Web version of this article.)

hours, UHII is analyzed by dividing into diurnal and nocturnal ones (Fig. 15). UHI phenomenon occupies more than 95 % of nighttime, with 0 °C–11.99 °C UHII, probably due to the urban canopy height model. The increased heat storage from an abundance of buildings in urban areas and reduced radiative cooling in urban canyons can contribute to significant nocturnal UHII. Compared to the nocturnal UHII, the diurnal UHII is reduced (UCII becomes significant), and approximately 61 % of daytime has a UHI phenomenon (0°C–12.10 °C). The rural areas in the daytime typically experience a more rapid warming. However, the blockage of solar radiation due to the building canopy and the heat storage increases the urban air temperature slowly, leading to more pronounced diurnal UCI phenomenon.

Following Figs. 16 and 17 show the spatial maps of temporal-averaged diurnal and nocturnal UHII, with periods focused on annual and seasonal durations.

The diurnal UHII is high in the northwestern and central parts with large building coverage. The temporal-averaged diurnal UHII is approximately 0.03 °C–0.90 °C for different seasons. Specifically, it is 0.08 °C–0.71 °C (annual), 0.06 °C–0.60 °C (spring), 0.07 °C–0.90 °C (summer), 0.03 °C–0.71 °C (autumn), and 0.13 °C–0.64 °C (winter) (Fig. 16a–e). When further averaging UHII throughout all blocks, the mean diurnal UHII is 0.19 °C, 0.16 °C, 0.19 °C, 0.16 °C, and 0.26 °C for the annual period, spring, summer, autumn, and winter. The seasonal variation coefficient can reach 62.50 % (winter vs. spring). Moreover, only the diurnal UHII of winter is above the annual average, whereas all other seasons is below or equal to the annual average.

The temporal-averaged nocturnal UHII is 1.27 °C–3.13 °C in different seasons (Fig. 17). Specifically, it is 1.72 °C–2.88 °C (annual period), 2.01 °C–3.03 °C (spring), 1.68 °C–3.13 °C (summer), 1.89 °C–2.99 °C (autumn), and 1.27 °C–2.34 °C (winter) (Fig. 17a–e). By

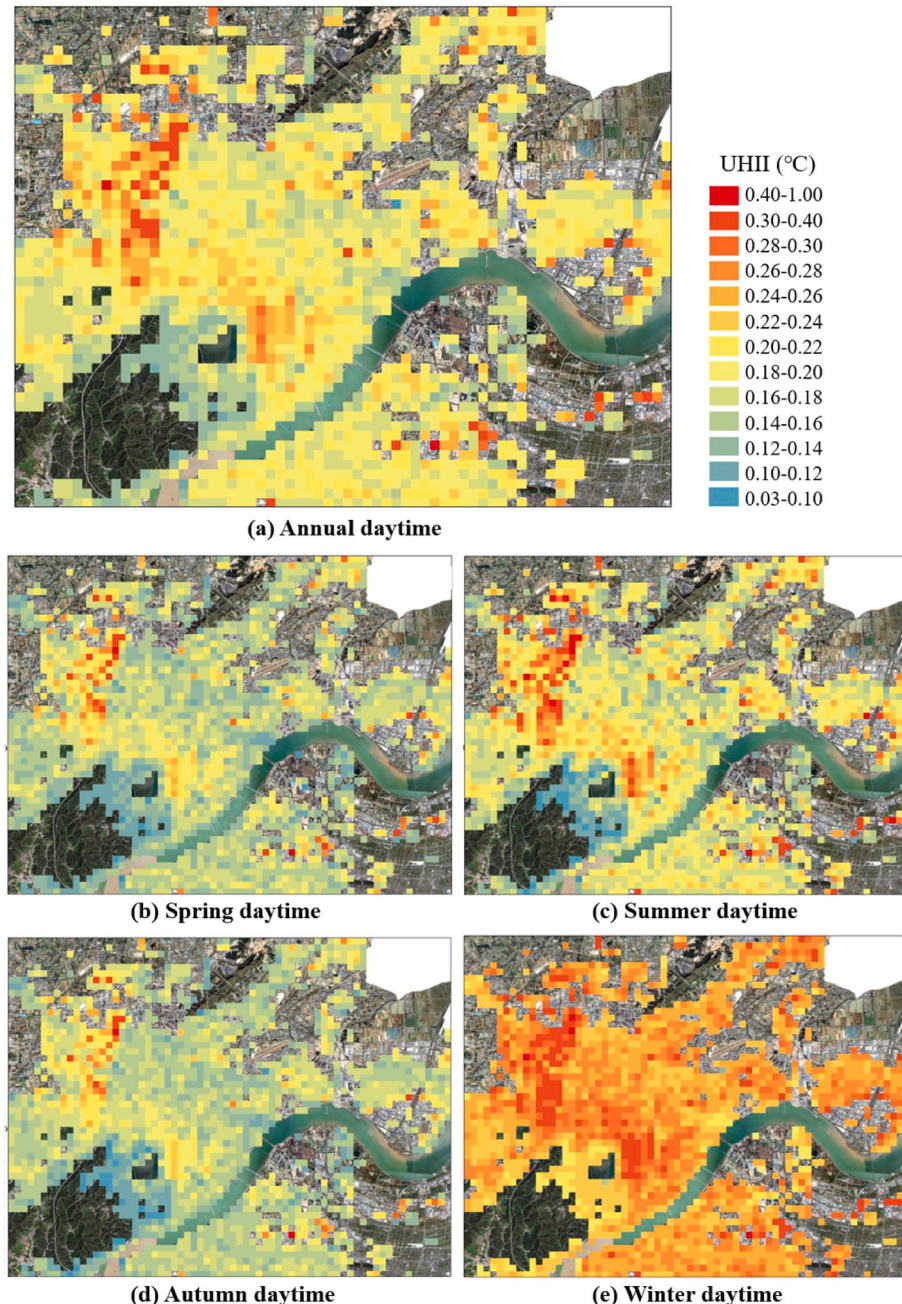


**Fig. 16.** Spatial maps of temporal-averaged diurnal urban heat island intensities (UHII) based on five periods: (a) annual; (b) spring; (c) summer; (d) autumn; (e) winter.

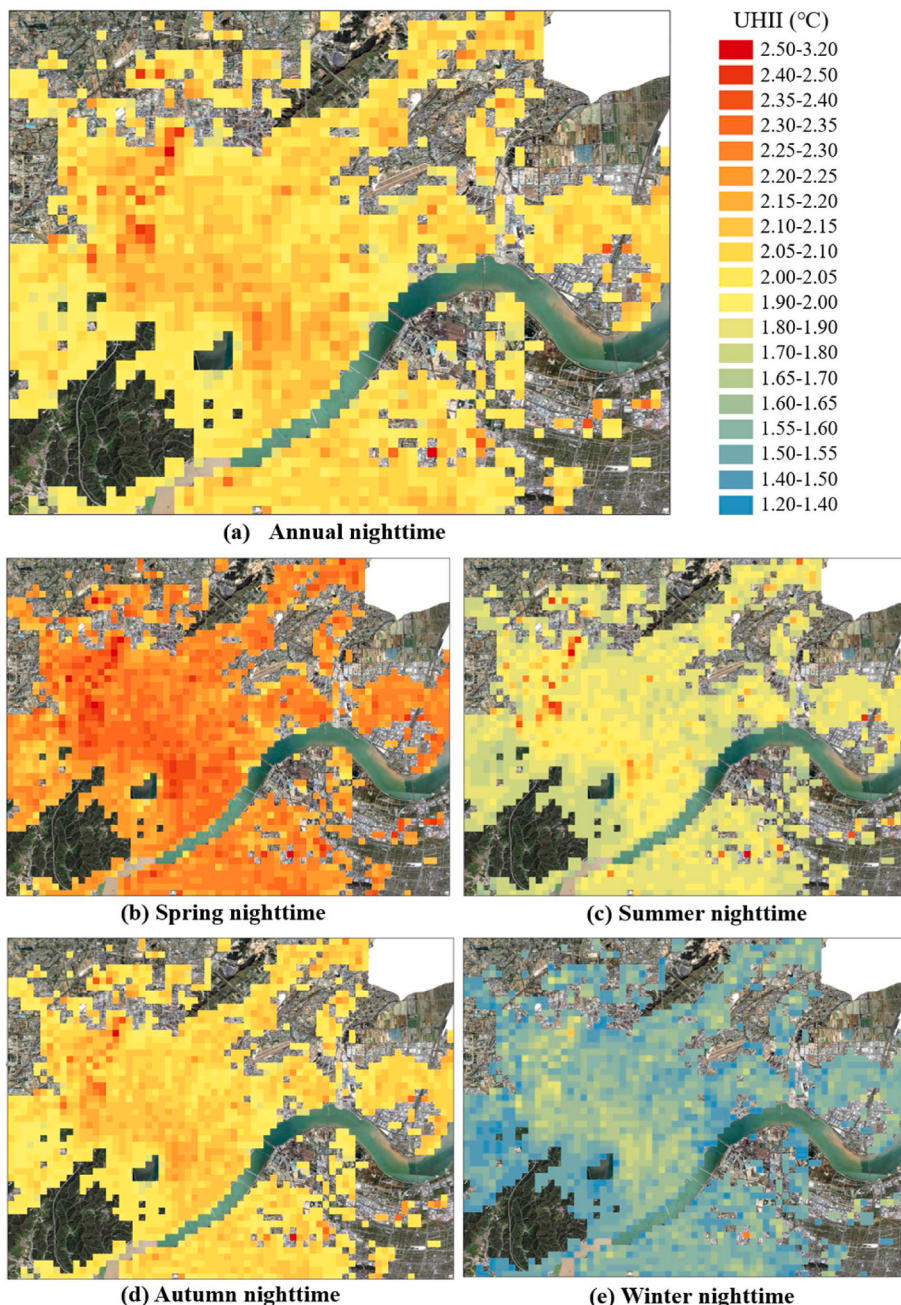


**Fig. 17.** Spatial maps of temporal-averaged nocturnal urban heat island intensities (UHII) based on five periods: (a) annual; (b) spring; (c) summer; (d) autumn; (e) winter.

further averaging all blocks, the nocturnal UHII are 2.06  $^{\circ}\text{C}$ , 2.36  $^{\circ}\text{C}$ , 2.01  $^{\circ}\text{C}$ , 2.22  $^{\circ}\text{C}$ , and 1.63  $^{\circ}\text{C}$  for the annual period, spring, summer, autumn, and winter. The seasonal variation coefficient can reach 44.80 % (spring vs. winter), consistent with UHII variation of a synthetic typical day (Fig. 14), indicating the greatest seasonal variation of nocturnal UHII between spring and winter.

### 3.2. Underlying surface effect on UHII

#### 3.2.1. LCZ map of Hangzhou City

This study investigates the underlying surface effect on UHII based on LCZ framework [26,74]. According to the LCZ classification by Stewart and Oke [26], morphological (e.g., building coverage, mean building height) and thermal properties are included to describe LCZ. However, not all the properties are available in this study, particularly

for all 1920 blocks over Hangzhou City. Since urban morphology is the most crucial for UHI study in UWG models [60], jointly considering the morphological parameter types in LCZ framework and data availability in this study, the building coverage and mean building height are selected for conducting the LCZ classification.

Practically, the building coverage and mean building height are calculated for all 1920 blocks. In some blocks, the calculated values cannot meet the defined ranges of any LCZ types (Table 2). Therefore, such blocks cannot be endowed with an LCZ type. Finally, eight LCZ types are identified in this study. Table 2 gives the defined property ranges and cumulative number of qualified blocks for each LCZ category.

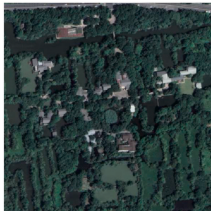
By assigning the classification results to blocks, Fig. 18 shows LCZ map for the built-up areas. LCZ 5 (open mid-rise) and LCZ 4 (open high-rise) dominate the studied area, accounting for 51.59 % and 11.46 %,

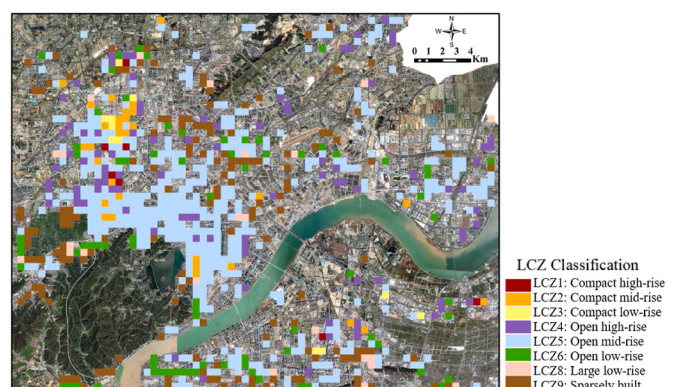
**Table 2**

Defined property ranges and collected amounts of eight identified local climate zone (LCZ) types in Hangzhou City.

LCZ type	Plan area density (%)	Mean building height (m)	Number of grids	Aerial view of one typical block
LCZ 1 Compact high-rise	40–60	>25	7 (0.85 %)	
LCZ 2 Compact mid-rise	40–70	10–25	31 (3.78 %)	
LCZ 3 Compact low-rise	40–70	3–10	11 (1.34 %)	
LCZ 4 Open high-rise	20–40	>25	94 (11.46 %)	
LCZ 5 Open mid-rise	20–40	10–25	423 (51.59 %)	

**Table 2 (continued)**

LCZ type	Plan area density (%)	Mean building height (m)	Number of grids	Aerial view of one typical block
LCZ 6 Open low-rise	20–30	3–10	77 (9.39 %)	
LCZ 8 Large low-rise	30–40	3–10	23 (2.80 %)	
LCZ 9 Sparsely built	10–20	3–10	154 (18.78 %)	

**Fig. 18.** Distribution map of available local climate zones (LCZs) in the studied built-up area.

respectively. LCZ 5 frequently appears in the city center, covering a large continuous area, whereas LCZ 4 is more geographically dispersed.

### 3.2.2. UHI features in different LCZs

This study characterizes LCZ by building coverage and mean building height. By doing statistical analysis of UHII in the blocks belonging to the same LCZ type, the seasonal-averaged diurnal and nocturnal UHII under different underlying surface types (represented by LCZs) are presented in Fig. 19 (y-axis range differs for Fig. 19a–d and Fig. 19e–h). In this study, LCZ 1 has the nearly highest building coverage

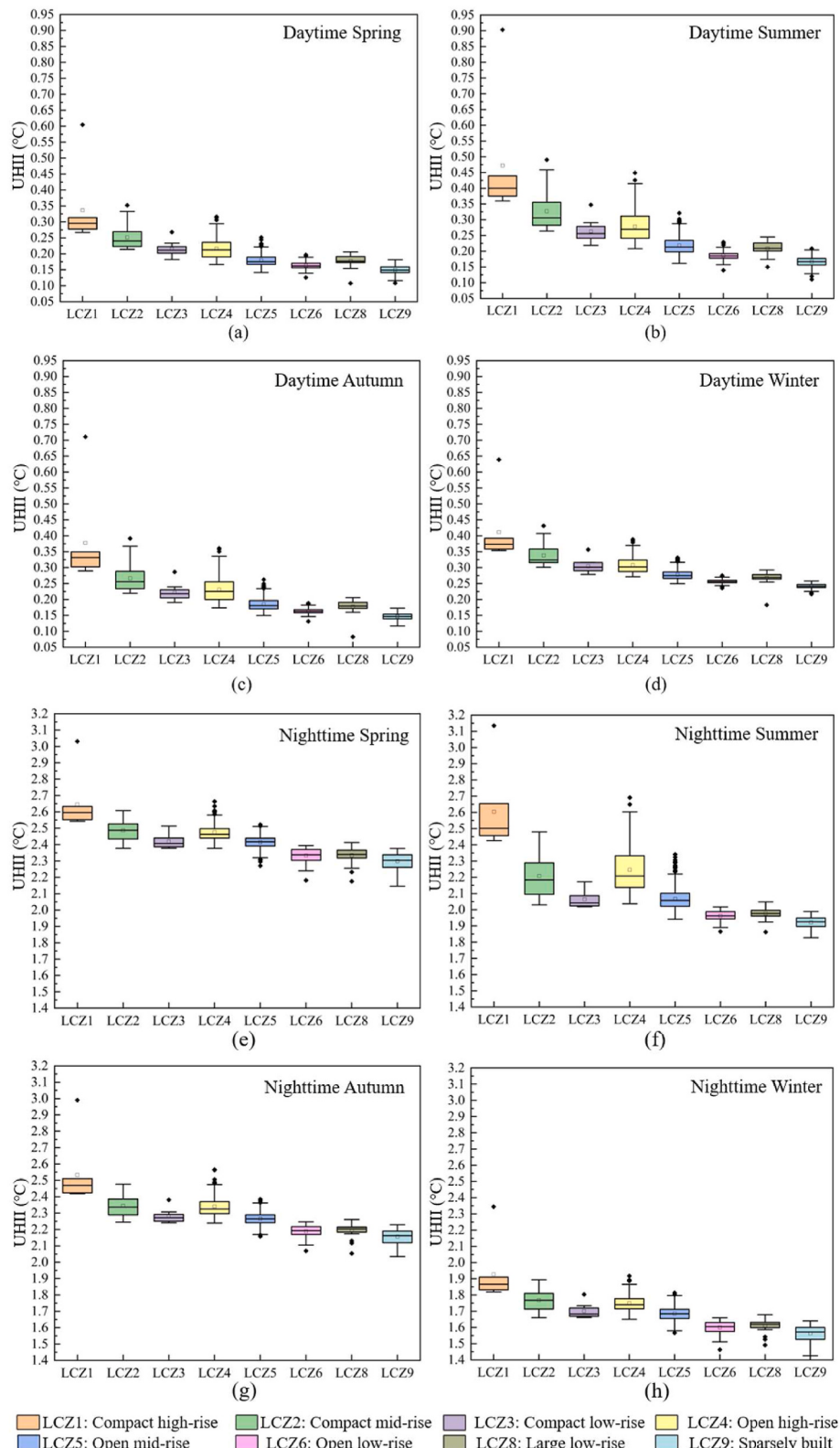


**Fig. 19.** Seasonal-averaged (a–d) diurnal and (e–h) nocturnal urban heat island intensities (UHII) at eight identified local climate zones (LCZs).

(approximately 46 %), mean building height (approximately 36 m), and the most significant UHII. The reverse is also true for LCZ 9.

For a clearer comparison, detailed data are partially given in Table 3, containing seasonal-averaged diurnal and nocturnal UHII for LCZs 1–6. Additionally, Table 3 also provides building coverage and mean building height information for LCZs 1–6.

Comparing UHII in the LCZ group with similar building coverage (compact group LCZs 1, 2, and 3, or open group LCZs 4, 5, 6), a positive correlation is observed between the mean building height and UHII. The building height influence is more significant for diurnal than nocturnal UHII. Taking the compact group (LCZs 1, 2, and 3) for example, the mean building height increased from 8.31 m in LCZ 3 to 35.91 m in LCZ

**Table 3**

Morphological parameters and urban heat island intensities (UHII) of LCZs 1–6; c: compact for LCZs 1, 2, 3; o: open for LCZs 4, 5, 6; h: high-rise for LCZs 1, 4); m: mid-rise for LCZs 2, 5; l: low-rise for LCZs 3, 6.

LCZ type	LCZ1 c, h	LCZ2 c, m	LCZ3 c, l	LCZ4 o, h	LCZ5 o, m	LCZ6 p, l
Building coverage (%)	45.63	46.24	46.60	25.98	26.47	24.30
Mean building height (m)	35.91	16.16	8.31	35.96	16.75	7.68
Diurnal UHII (°C)	Spring	0.34	0.25	0.22	0.22	0.16
	Summer	0.47	0.33	0.26	0.28	0.19
	Autumn	0.38	0.27	0.22	0.23	0.16
	Winter	0.41	0.34	0.30	0.31	0.26
Nocturnal UHII (°C)	Spring	2.65	2.49	2.42	2.48	2.42
	Summer	2.60	2.21	2.07	2.25	2.07
	Autumn	2.53	2.34	2.28	2.34	2.27
	Winter	1.93	1.77	1.70	1.75	1.69

1. Correspondingly, the diurnal UHII is improved by approximately 137 % (i.e., increased from 0.30 °C to 0.41 °C, calculated as 0.41/0.30, similarly after this) in winter or can be even approximately 181 % (0.47/0.26) in summer. However, the increase rate is lower for nocturnal UHII, approximately 114 % (1.93/1.70) in winter and 126 % (2.60/2.07) in summer.

Moreover, the building height influence is more distinguished in the compact group, compared to the open one. The maximum diurnal UHII improvement in the open group is approximately 147 % (0.28/0.19, summer diurnal UHII), lower than 181 % (0.47/0.26, summer diurnal UHII) in the compact group.

When exploring the building coverage influence by examining UHII in the LCZ group with similar mean building heights (high-rise group LCZs 1 and 4, mid-rise group LCZs 2 and 5, or low-rise group LCZs 3 and 6), the higher building coverage is typically accompanied with a more evident UHI phenomenon. Stewart and Oke [26] have reported similar findings. Again, the building coverage influence is more significant for the diurnal than nocturnal UHII. For example, in the high-rise group (LCZs 1 and 4), the diurnal UHII improves at least 132 % (0.41/0.31, in winter) to a maximum of approximately 168 % (0.47/0.28, in summer) when the building coverage increased from approximately 26 %–46 %; the increased rate is lower for the nocturnal UHII of the same group, from 110 % (1.93/1.75, in winter) to 116 % (2.60/2.25, in summer).

Moreover, the building coverage influence is more crucial in the high-rise group than the low-rise group. Taking the summer diurnal UHII for example, the maximum increase rate is approximately 168 % (0.47/0.28) in the high-rise group, compared to approximately 137 % (0.26/0.19) in the low-rise group.

### 3.2.3. Relation between underlying surface parameters and UHII

By statistically analyzing the morphological information in each 500 × 500 m<sup>2</sup> block, the influence of building coverage, vegetation ratio, and building height on the annual average UHII is explored. The relationship and basic correlation coefficient between individual parameters and UHII are quantified (Fig. 20). Other statistical methods, e.g., analysis of variance (ANOVA) for analyzing the differences between means of different groups and the Morris method for global sensitivity analysis, can be employed for next-phase studies, if applicable.

UHII shows approximate linear relationships with the building coverage or vegetation coverage (Fig. 20a and b). Particularly, the annual average UHII positively improves with the building coverage, with a correlation coefficient of 0.76 (Fig. 20a). The specific fitting law between the annual average UHII ( $y$ ) and building coverage ( $x_{bc}$ ) is  $y = 0.45x_{bc} + 1.06$ . This high correlation coefficient indicates the significant sensitivity of UHII to the building coverage, consistent with the previous studies [56,60] that maintained building coverage is one of the most influential factors for UHII. Consequently, the neighborhood-scale UHII can be effectively regulated by controlling the building coverage.

The annual average UHII ( $y$ ) is negatively correlated to the

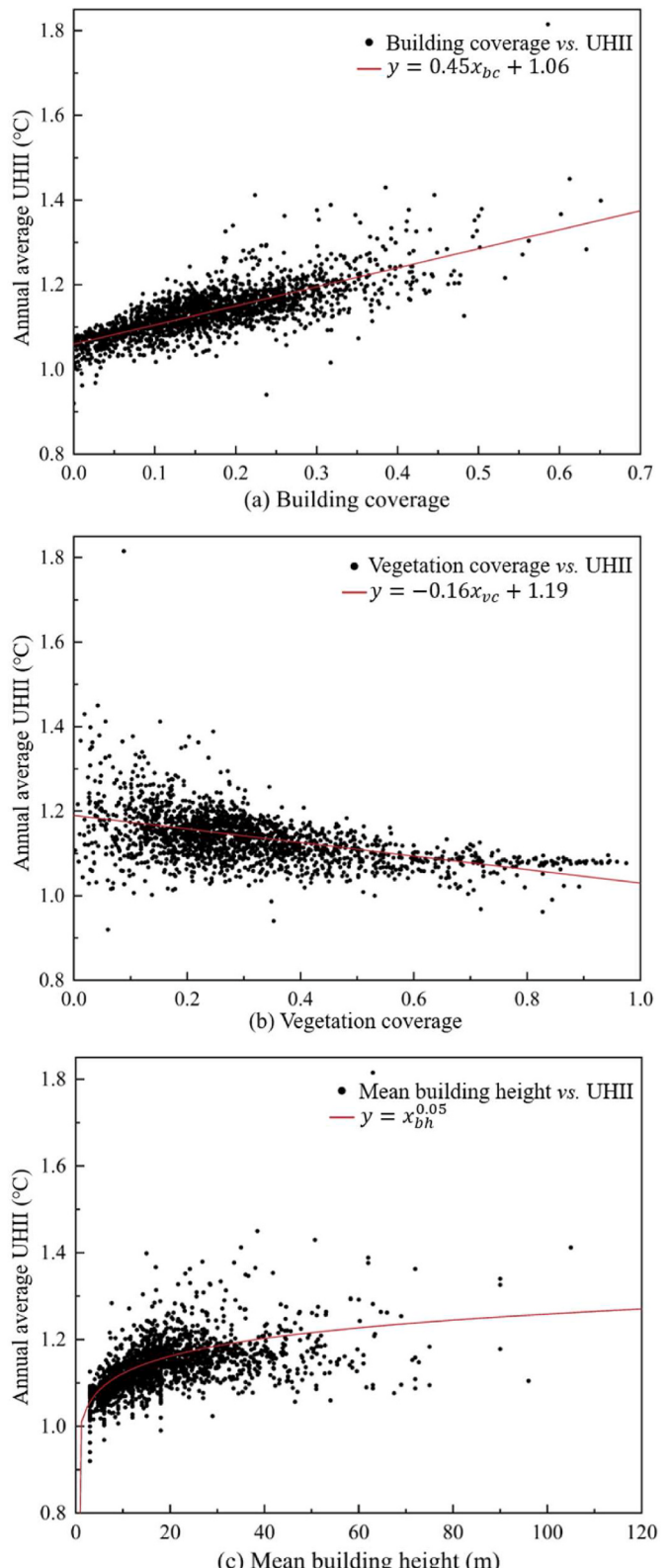


Fig. 20. Relations between annual average urban heat island intensity (UHII) and different urban underlying surface parameters: (a) building coverage; (b) vegetation coverage, and (c) mean building height.

vegetation coverage ( $x_{vc}$ ), with a bulk correlation coefficient of  $-0.48$  and a fitting law of  $y = -0.16x_{vc} + 1.19$  (Fig. 20b). The local correlation is significant when the vegetation ratio is high. However, UHII scatters are dispersive when the vegetation coverage is low, implying that other factors may dominate UHII. By expanding the vegetation coverage range with a step of  $0.10$ , the local correlation coefficients in different sections ( $[0.50, 1.00]$ ,  $[0.40, 1.00]$ ,  $[0.30, 1.00]$ ,  $[0.20, 1.00]$ ,  $[0.10, 1.00]$ ,  $[0, 1.00]$ ) are analyzed, where the range  $[0.50, 1.00]$  is the reference range. The correlation coefficient can approach a negative peak of approximately  $-0.51$  when the range extends to  $[0.20, 1.00]$ , beyond which the correlation recedes. This indicates the important role of vegetation coverage when it is beyond  $20\%$ . Therefore, vegetation coverage is suggested to be larger than  $20\%$  for UHI mitigation.

The relationship between annual average UHII ( $y$ ) and mean building height ( $x_{bh}$ ) is shifted away from a basic linear relationship and is much closer to a power-law increase, with a fitted formula of  $y = x_{bh}^{0.05}$  (Fig. 20c). Similarly, taking the height interval of  $10\text{ m}$ , the local correlation coefficients in different height sections ( $[0, 10]$ ,  $[0, 20]$ ,  $[0, 30]$ , ...) are analyzed. The maximum positive correlation coefficient is  $0.63$  in the  $[0, 20]$  section, indicating that a strong UHII relation to building height exists in the low-rise and mid-rise building groups. When the mean building height is higher than  $20\text{ m}$ , other factors become more crucial to UHII.

#### 4. Discussions

This study combined UWG and LCZ to explore the hourly UHII under various underlying surface characteristics in Hangzhou City. The most crucial originality of this study lies in the fact that UWG simulation was applied over the entire primary urban area for the whole year, not limited to several representative blocks or some typical short periods. This achievement relies on deep-learning methods to identify underlying surface types and the automatic cyclical simulation of UWG models to improve the simulation efficiency.

The study demonstrates that the performance of UWG is comparable to existing studies by giving an average RMSE of  $0.78\text{ }^{\circ}\text{C}$  for monthly comparisons and  $0.66\text{ }^{\circ}\text{C}$  for annual comparisons. Some interesting phenomena are observed in spring. It has the highest annual UHII among the four seasons, mainly related to the lower rural temperature induced by soil thermal inertia. UHI and UCI phenomena are simultaneously strengthened in spring, compared to winter.

This study generates annual and seasonal UHI maps, endorsing essential urban areas with urgent UHI mitigation needs. The hotspot identification from UHI maps would also help evaluate the heat exposure of residents and locate vulnerable sites and populations more precisely. The study justifies that UHII is closely related to the underlying surface parameters. High-UHII areas are primarily in the central region with compact building groups. Low-UHII areas are primarily found in high-vegetation-coverage regions. By adopting LCZ framework to classify the underlying surface types, LCZ 1 (compact high-rise configurations) has the highest UHII, independent of the examined periods (seasonal daytime/nighttime). For future urban planning, the percentage of compact high-rise configurations (LCZ 1) in the urban area shall be limited to control the overall UHII magnitude.

This study verifies that building coverage has the highest influence on UHII compared to building height and vegetation coverage. The building coverage particularly affects UHII in the high-rise building group, with a maximum improvement of approximately  $168\%$  for the summer diurnal UHII. The correlation between building coverage and annual UHII can reach  $0.76$ . Therefore, the neighborhood-scale UHII can be effectively regulated by controlling the building coverage. The mean building height and vegetation coverage have specific scopes where their performance on UHII modulation is significant. Specifically, building height contributes more to UHII in low-rise and mid-rise building groups (the mean height is less than  $20\text{ m}$ ). The vegetation coverage is more effective when it is beyond  $20\%$ . In this way, proper

mitigating methods can be chosen to achieve desirable urban thermal environment for different urban zones.

This study has several major limitations, as follows:

First, in UWG simulation, the primary input required for UHI study includes building characteristics, vegetation ratio, and anthropogenic heat (e.g., building and traffic heat emission). As a crucial influencing factor, anthropogenic heat data use the default value in the models, whereas the accurate value of each block is not collected in this study. Therefore, the impact of varied anthropogenic heat on spatiotemporal UHII is yet to be evaluated. Future work should focus on the quantitative analysis of the anthropogenic heat and its influence on the urban thermal environment to fully understand UHI regulation and mitigation. The following strategies can be considered to obtain the anthropogenic heat data: (1) using anthropogenic heat emission data from local government or city agency (2) using remote sensing technologies (e.g., satellite imagery, aerial surveys, thermal infrared imaging, etc.) to assess heat emissions from urban areas, and (3) conducting a comprehensive literature review to find existing measurements or estimation data of anthropogenic heat emissions in similar urban contexts as a reference.

Second, building coverage, building height, and vegetation coverage, as three crucial influencing factors, are studied to find their correlation with UHII in all blocks. However, a more comprehensive analysis of the influence of meteorological parameters and other underlying surface parameters on UHII is expected. Studying the coupling effect of multiple factors to propose UHI mitigation strategies for Hangzhou City would be valuable.

Third, this study uses two urban morphological parameters, building coverage and mean building height, for LCZ classification. Other properties (e.g., sky view factor, canyon aspect ratio, etc.) are not included. Future studies will be interesting if more underlying surface parameters are derived to further improve the LCZ classification.

Last, this paper takes Hangzhou City as the study example. Methodologies could be applied to analyze UHI in other climate zones, and the underlying physical mechanisms would be similar. However, the quantitative spatiotemporal characteristics might show different patterns. It will be interesting to extend this study to other megacities in different climatic zones for future work.

#### 5. Conclusions

This study proposed a framework, incorporated by UWG, LCZ, deep-learning methods, and Python automatic cyclical calculation, to derive the annual hourly (total  $8760\text{ h}$ ) UHII at the LCZ scale ( $500 \times 500\text{ m}^2$ ) over the entire primary urban area (total  $1920$  blocks) of Hangzhou City. UHI maps at annual and seasonal scales and corresponding synthetic daily 24-h UHII are obtained. UHII features in various LCZs and their relationship with urban underlying surface parameters are quantified.

The primary results are summarized as follows.

- (1) In more than  $96\%$  time ( $8760\text{ h}$ ), the spatial-averaged hourly UHII were between  $-2\text{ }^{\circ}\text{C}$  and  $6\text{ }^{\circ}\text{C}$ , and those at  $0\text{ }^{\circ}\text{C}-1\text{ }^{\circ}\text{C}$  contribute  $43.80\%$  of the total time. Spring gives the most intense nocturnal UHII, whereas winter has the weakest one. A significant diurnal UCI phenomenon could accompany the strong nocturnal UHI phenomenon. From the synthetic (based on seasonal data) 24-h curves, mean UHII and UCII (average of the positive and negative values, respectively) drop by approximately  $25\%$  in winter compared to spring.
- (2) UHII is higher in the central region with compact buildings but significantly lower in the high-vegetation-coverage region. LCZ 1 has the highest UHII, independent of the examined periods (seasonal daytime/nighttime). The relationship between LCZ and seasonal-averaged diurnal/nocturnal UHII demonstrates that the building height influence is more important in the compact building group, compared to the open one. The building coverage

- impact is more crucial in the high-rise building group, compared to the low-rise one.
- (3) Building coverage has the highest influence on the annual average UHII, with a positive correlation coefficient of 0.76. The power-law increase and negative correlation of annual average UHII are found for the mean building height and vegetation coverage, respectively. The building height contributes more to UHII in low-rise and mid-rise building groups (the mean height is less than 20 m), and the vegetation coverage starts to play a particularly crucial role in UHII when it is beyond 20 %.

This study should be of great interest to urban planners to identify the fundamental urban areas with urgent UHI mitigation needs and enhance the understanding of the relationship between underlying surface parameters and UHII. It provides straightforward quantitative data to support the strategies to mitigate the UHII by controlling critical morphological parameters, such as limiting the percentage of LCZ 1 configurations to control the overall UHII magnitude, adjusting building coverage to regulate neighborhood-scale UHII, and increasing vegetation coverage beyond 20 % to reduce UHII. Future studies should further consider the impact of anthropogenic heat on UHII and analyze UHII under the coupling effect of meteorological parameters and other morphological factors.

#### CRediT authorship contribution statement

**Shi Yin:** Writing – review & editing, Supervision, Resources, Project administration, Methodology, Investigation, Funding acquisition, Formal analysis, Conceptualization. **Songyi Xiao:** Writing – original draft, Validation, Software, Methodology, Investigation, Formal analysis. **Xiaotian Ding:** Software, Methodology. **Yifan Fan:** Writing – review & editing, Supervision, Resources, Project administration, Funding acquisition, Conceptualization.

#### Declaration of competing interest

The authors declare that they have no known competing financial interests or personal relationships that could have appeared to influence the work reported in this paper.

#### Data availability

Data sharing is not applicable currently because other research analysis based on this data is performing.

#### Acknowledgments

This study is supported by the National Natural Science Foundation of China (No. 52208130), “Pioneer” and “Leading Goose” R&D Program of Zhejiang (No. 2023C03152), Zhejiang Provincial Natural Science Foundation of China (No. LQ21E080014), Fundamental Research Funds for the Central Universities (No. 226-2022-00029), and Opening Fund of State Key Laboratory of Green Building (No. LSKF202204).

#### References

- [1] United Nations, Department of Economic and Social Affairs, Population Division. *World Urbanization Prospects: the 2018 Revision*, United Nations, New York, 2019.
- [2] K.L. Finell, A. Berg, P. Gentine, J.P. Krasting, B.R. Lintner, S. Malyshov, J. A. Santanello Jr., E. Sheviakova, The impact of anthropogenic land use and land cover change on regional climate extremes, *Nat. Commun.* 8 (1) (2017) 989.
- [3] Z. Mokhtari, M. Amani-Beni, A. Asgarian, A. Russo, S. Qureshi, A. Karimi, Spatial prediction of the urban inter-annual land surface temperature variability: an integrated modeling approach in a rapidly urbanizing semi-arid region, *Sustain. Cities Soc.* 93 (2023), 104523.
- [4] P. Rajagopal, R.S. Priya, R. Senthil, A review of recent developments in the impact of environmental measures on urban heat island, *Sustain. Cities Soc.* 88 (2023), 104279.
- [5] T.R. Oke, G. Mills, A. Christen, J.A. Voogt, *Urban Climates*, Cambridge University Press, 2017.
- [6] L.W.A. van Hove, C.M.J. Jacobs, B.G. Heusinkveld, J.A. Elbers, B.L. van Driel, A.A. M. Holtslag, Temporal and spatial variability of urban heat island and thermal comfort within the rotterdam agglomeration, *Build. Environ.* 83 (2015) 91–103.
- [7] G. Battista, L. Evangelisti, C. Guattari, M. Roncone, C.A. Balaras, Space-time estimation of the urban heat island in Rome (Italy): overall assessment and effects on the energy performance of buildings, *Build. Environ.* 228 (2023), 109878.
- [8] L. Zhao, M. Oppenheimer, Q. Zhu, J.W. Baldwin, K.L. Ebi, E. Bou-Zeid, K. Guan, X. Liu, Interactions between urban heat islands and heat waves, *Environ. Res. Lett.* 13 (3) (2018), 034003.
- [9] H.L. Macintyre, C. Heaviside, X. Cai, R. Phalkey, Comparing temperature-related mortality impacts of cool roofs in winter and summer in a highly urbanized European region for present and future climate, *Environ. Int.* 154 (2021), 106606.
- [10] A. Piracha, M.T. Chaudhary, Urban air pollution, urban heat island and human health: a review of the literature, *Sustainability* 14 (15) (2022) 9234.
- [11] V. Sangiorgio, F. Fiorito, M. Santamouris, Development of a holistic urban heat island evaluation methodology, *Sci. Rep.* 10 (2020), 17913.
- [12] G. Xu, H. Zhao, J. Li, Y. Shi, X. Feng, Y. Zhang, Multivariate thermal environment data extraction and evaluation: a neighborhood scale case in Guangzhou, China, *Build. Environ.* 234 (2023), 110190.
- [13] M. Anjos, A.C. Targino, P. Krecl, G.Y. Oukawa, R.F. Braga, Analysis of the urban heat island under different synoptic patterns using local climate zones, *Build. Environ.* 185 (2020), 107268.
- [14] J. Lin, S. Qiu, X. Tan, Y. Zhuang, Measuring the relationship between morphological spatial pattern of green space and urban heat island using machine learning methods, *Build. Environ.* 228 (2023), 109910.
- [15] Y. Shi, Y. Zhang, Urban morphological indicators of urban heat and moisture islands under various sky conditions in a humid subtropical region, *Build. Environ.* 214 (2022), 108906.
- [16] J. Ren, K. Shi, X. Kong, H. Zhou, On-site measurement and numerical simulation study on characteristic of urban heat island in a multi-block region in Beijing, China, *Sustain. Cities Soc.* 95 (2023), 104615.
- [17] Y. Kim, S. Yu, D. Li, S.N. Gatson, R.D. Brown, Linking landscape spatial heterogeneity to urban heat island and outdoor human thermal comfort in Tokyo: application of the outdoor thermal comfort index, *Sustain. Cities Soc.* 87 (2022), 104262.
- [18] M. Singh, R. Sharston, Quantifying the dualistic nature of urban heat island effect (UHI) on building energy consumption, *Energy Build.* 255 (2022), 111649.
- [19] M. Palme, L. Inostroza, G. Villares, A. Lobato-Cordero, C. Carrasco, From urban climate to energy consumption: Enhancing building performance simulation by including the urban heat island effect, *Energy Build.* 145 (2017) 107–120.
- [20] X. Li, Y. Zhou, S. Yu, G. Jia, H. Li, W. Li, Urban heat island impacts on building energy consumption: a review of approaches and findings, *Energy* 174 (2019) 407–419.
- [21] Y. Yang, Q. Gu, H. Wei, H. Liu, W. Wang, S. Wei, Transforming and validating urban microclimate data with multi-sourced microclimate datasets for building energy modelling at urban scale, *Energy Build.* 295 (2023), 113318.
- [22] Y. Liu, Q. Li, L. Yang, K. Mu, M. Zhang, J. Liu, Urban heat island effects of various urban morphologies under regional climate conditions, *Sci. Total Environ.* 743 (2020), 140589.
- [23] T. Loridan, C.S.B. Grimmond, Characterization of energy flux partitioning in urban environments: links with surface seasonal properties, *J. Appl. Meteorol. Climatol.* 51 (2) (2012) 219–241.
- [24] C. Ren, E.Y.Y. Ng, L. Katschner, Urban climatic map studies: a review, *Int. J. Climatol.* 31 (15) (2011) 2213–2233.
- [25] B. Han, Z. Luo, Y. Liu, T. Zhang, L. Yang, Using local climate zones to investigate spatio-temporal evolution of thermal environment at the urban regional level: a case study in xi'an, China, *Sustain. Cities Soc.* 76 (2022), 103495.
- [26] I.D. Stewart, T.R. Oke, Local climate zones for urban temperature studies, *Bull. Am. Meteorol. Soc.* 93 (12) (2012) 1879–1900.
- [27] X. Zhang, G.J. Steeneveld, D. Zhou, R.J. Ronda, C. Duan, S. Koopmans, A.A. M. Holtslag, Modelling urban meteorology with increasing refinements for the complex morphology of a typical Chinese city (Xi'an), *Build. Environ.* 182 (2020), 107109.
- [28] R. Kotharkar, A. Bagade, Local Climate Zone Classification for Indian Cities: A Case Study of Nagpur, *Urban Clim.* 24 (2018) 369–392.
- [29] L. Ramakrishnan, N. Aghamohammadi, C.S. Fong, A. Ghaffarianhoseini, A. Ghaffarianhoseini, L.P. Wong, N. Hassan, N.M. Sulaiman, A Critical Review of Urban Heat Island Phenomenon in the Context of Greater Kuala Lumpur, Malaysia, *Sustain. Cities Soc.* 39 (2018) 99–113.
- [30] X. Yang, L. Yao, T. Jin, L.L.H. Peng, Z. Jiang, Z. Hu, Y. Ye, Assessing the Thermal Behavior of Different Local Climate Zones in the Nanjing Metropolis, China, *Build. Environ.* 137 (2018) 171–184.
- [31] Y. Zheng, C. Ren, Y. Shi, S.H.L. Yim, D.Y.F. Lai, Y. Xu, C. Fang, W. Li, Mapping the Spatial Distribution of Nocturnal Urban Heat Island Based on Local Climate Zone Framework, *Build. Environ.* 234 (2023), 110197.
- [32] Y. Chen, J. Li, Y. Hu, L. Liu, Spatial and Temporal Characteristics of Nighttime UHII Based on Local Climate Zone Scheme Using Mobile Measurement-a Case Study of Changsha, *Build. Environ.* 228 (2023), 109869.
- [33] P. Du, J. Chen, X. Bai, W. Han, Understanding the Seasonal Variations of Land Surface Temperature in Nanjing Urban Area Based on Local Climate Zone, *Urban Clim.* 33 (2020), 100657.
- [34] A. Rodler, T. Leduc, Local Climate Zone Approach on Local and Micro Scales: Dividing the Urban Open Space, *Urban Clim.* 28 (2019), 100457.

- [35] C. Beck, A. Straub, S. Breitner, J. Cyrys, A. Philipp, J. Rathmann, A. Schneider, K. Wolf, J. Jacobbeit, Air Temperature Characteristics of Local Climate Zones in the Augsburg Urban Area (Bavaria, Southern Germany) under Varying Synoptic Conditions, *Urban Clim.* 25 (2018) 152–166.
- [36] S. Caluwaerts, R. Hamdi, S. Top, D. Lauwaet, J. Berckmans, D. Degrauwé, H. Dejonghe, K. De Ridder, R. De Troch, F. Duchêne, B. Maiheu, M. Van Ginderachter, M.-L. Verdonck, T. Vergauwen, G. Wauters, P. Termonia, The Urban Climate of Ghent, Belgium: A Case Study Combining a High-Accuracy Monitoring Network with Numerical Simulations, *Urban Clim.* 31 (2020), 100565.
- [37] Y. Shi, K.K.L. Lau, C. Ren, E. Ng, Evaluating the Local Climate Zone Classification in Highdensity Heterogeneous Urban Environment Using Mobile Measurement, *Urban Clim.* 25 (2018) 167–186.
- [38] I.D. Stewart, T.R. Oke, E.S. Krayenhoff, Evaluation of the ‘Local Climate Zone’ Scheme Using Temperature Observations and Model Simulations, *Int. J. Climatol.* 34 (4) (2014) 1062–1080.
- [39] X. Zhou, T. Okaze, C. Ren, M. Cai, Y. Ishida, H. Watanabe, A. Mochida, Evaluation of Urban Heat Islands Using Local Climate Zones and the Influence of Sea-Land Breeze, *Sustain. Cities Soc.* 55 (2020), 102060.
- [40] W.Z. Zhang, H.Y. Huo, X.W. Geng, P. Zhou, L. Guo, Z.L. Li, Simulation of Canopy Urban Heat Island at a Block Scale Based on Local Climatic Zones and Urban Weather Generator: A Case Study of Beijing, *Int. J. Rem. Sens.* (2023), <https://doi.org/10.1080/01431161.2023.2203344>.
- [41] M. Chäfer, C.L. Tan, R.J. Cureau, W.N. Hien, A.L. Pisello, L.F. Cabeza, Mobile Measurements of Microclimatic Variables through the Central Area of Singapore: An Analysis from the Pedestrian Perspective, *Sustain. Cities Soc.* 83 (2022), 103986.
- [42] O. Aleksandrowicz, D. Pearlmuter, The Significance of Shade Provision in Reducing Street-Level Summer Heat Stress in a Hot Mediterranean Climate, *Landsc. Urban Plann.* 229 (2023), 104588.
- [43] A. Cecilia, G. Casasanta, I. Petenko, A. Conidi, S. Argentini, Measuring the Urban Heat Island of Rome through a Dense Weather Station Network and Remote Sensing Imperviousness Data, *Urban Clim.* 47 (2023), 101355.
- [44] d.S.E. Nikolai, A.C.d.S. Carlos, B.L.d.O. Maria, T.S. Madson, A.G.S. Celso, M.d. S. Richard, M. Manoranjan, R.F. Rosaria, Assessment of Urban Heat Islands and Thermal Discomfort in the Amazonia Biome in Brazil: A Case Study of Manaus City, *Build. Environ.* 227 (2023), 109772.
- [45] Z. Zou, C. Yan, L. Yu, X. Jiang, J. Ding, L. Qin, B. Wang, G. Qiu, Impacts of Land Use/Land Cover Types on Interactions between Urban Heat Island Effects and Heat Waves, *Build. Environ.* 204 (2021), 108138.
- [46] J. Yuan, S. Masuko, Y. Shimazaki, T. Yamanaka, T. Kobayashi, Evaluation of Outdoor Thermal Comfort under Different Building External-Wall-Surface with Different Reflective Directional Properties Using CFD Analysis and Model Experiment, *Build. Environ.* 207 (2022), 108478.
- [47] R. Zhang, P.A. Mirzaei, B. Jones, Development of a Dynamic External CFD and BES Coupling Framework for Application of Urban Neighbourhoods Energy Modelling, *Build. Environ.* 146 (2018) 37–49.
- [48] E. Morini, A.G. Touchaei, F. Rossi, F. Cotana, H. Akbari, Evaluation of Albedo Enhancement to Mitigate Impacts of Urban Heat Island in Rome (Italy) Using WRF Meteorological Model, *Urban Clim.* 24 (2018) 551–566.
- [49] X.X. Li, L.K. Norford, Evaluation of Cool Roof and Vegetations in Mitigating Urban Heat Island in a Tropical City, Singapore, *Urban Clim.* 16 (2016) 59–74.
- [50] M.O. Mughal, X.X. Li, L.K. Norford, Urban Heat Island Mitigation in Singapore: Evaluation Using WRF/Multilayer Urban Canopy Model and Local Climate Zones, *Urban Clim.* 34 (2020), 100714.
- [51] X. Wang, H. Li, S. Sodoudi, The Effectiveness of Cool and Green Roofs in Mitigating Urban Heat Island and Improving Human Thermal Comfort, *Build. Environ.* 217 (2022), 109082.
- [52] B. Bueno, L. Norford, J. Hidalgo, G. Pigeon, The Urban Weather Generator, *Journal of Building Performance Simulation* 6 (4) (2013) 269–281.
- [53] B. Bueno, M. Roth, L. Norford, R. Li, Computationally Efficient Prediction of Canopy Level Urban Air Temperature at the Neighbourhood Scale, *Urban Clim.* 9 (2014) 35–53.
- [54] S. Martinez, A. Machard, A. Pellegrino, K. Touili, L. Servant, E. Bozonnet, A Practical Approach to the Evaluation of Local Urban Overheating—A Coastal City Case-Study, *Energy Build.* 253 (2021), 111522.
- [55] G. Xu, J. Li, Y. Shi, X. Feng, Y. Zhang, Improvements, Extensions, and Validation of the Urban Weather Generator (UWG) for Performance-Oriented Neighborhood Planning, *Urban Clim.* 45 (2022), 101247.
- [56] J. Litardo, M. Palme, M. Borbor-Cordova, R. Caiza, J. Macias, R. Hidalgo-Leon, G. Soriano, Urban Heat Island Intensity and Buildings’ Energy Needs in Duran, Ecuador: Simulation Studies and Proposal of Mitigation Strategies, *Sustain. Cities Soc.* 62 (2020), 114279.
- [57] P. Shen, M. Wang, J. Liu, Y. Ji, Hourly Air Temperature Projection in Future Urban Area by Coupling Climate Change and Urban Heat Island Effect, *Energy Build.* 279 (2023), 112676.
- [58] A. Salvati, P. Monti, H. Coch Roura, C. Cecere, Climatic Performance of Urban Textures: Analysis Tools for a Mediterranean Urban Context, *Energy Build.* 185 (2019) 162–179.
- [59] A. Boccalatte, M. Fossa, M. Thebaud, J. Ramousse, C. Ménézo, Mapping the Urban Heat Island at the Territory Scale: An Unsupervised Learning Approach for Urban Planning Applied to the Canton of Geneva, *Sustain. Cities Soc.* 96 (2023), 104677.
- [60] A. Salvati, M. Palme, L. Inostroza, Key Parameters for Urban Heat Island Assessment in A Mediterranean Context: A Sensitivity Analysis Using the Urban Weather Generator Model, *IOP Conf. Ser. Mater. Sci. Eng.* 245 (2017), 082055.
- [61] M. Kottek, J. Grieser, C. Beck, B. Rudolf, F. Rubel, World Map of the Köppen-Geiger Climate Classification Updated, *Meteorol. Z.* 15 (3) (2006) 259–263.
- [62] X. Yang, L.L.H. Peng, Z. Jiang, Y. Chen, L. Yao, Y. He, T. Xu, Impact of Urban Heat Island on Energy Demand in Buildings: Local Climate Zones in Nanjing, *Appl. Energy* 260 (2020), 114279.
- [63] L. Schibuola, C. Tambani, Performance Assessment of Seawater Cooled Chillers to Mitigate Urban Heat Island, *Appl. Therm. Eng.* 175 (2020), 115390.
- [64] ASHRAE, Climatic Data for Building Design, In (Vol. ANSI/ASHRAE Standard 169-2013): ASHRAE, 2013.
- [65] U.B. Bueno, An Urban Weather Generator Coupling a Building Simulation Program with an Urban Canopy Model. (Master Degree), Massachusetts Institute of Technology, MA, USA, 2010.
- [66] Z. Li, Z.W. Yan, Y.N. Zhu, N. Freychet, S. Tett, Homogenized Daily Relative Humidity Series in China during 1960–2017, *Adv. Atmos. Sci.* 37 (4) (2020) 318–327.
- [67] Y. Fan, X. Ding, J. Wu, J. Ge, Y. Li, High Spatial-Resolution Classification of Urban Surfaces Using a Deep Learning Method, *Build. Environ.* 200 (2021), 107949.
- [68] B.J. He, J. Wang, H. Liu, G. Ulpiani, Localized Synergies between Heat Waves and Urban Heat Islands: Implications on Human Thermal Comfort and Urban Heat Management, *Environ. Res.* 193 (2021), 110584.
- [69] H. Kim, D. Gu, H.Y. Kim, Effects of Urban Heat Island Mitigation in Various Climate Zones in the United States, *Sustain. Cities Soc.* 41 (2018) 841–852.
- [70] X.Y. Yang, Y.G. Li, Z.W. Luo, P.W. Chan, The Urban Cool Island Phenomenon in a High-Rise High-Density City and Its Mechanisms, *Int. J. Climatol.* 37 (2) (2017) 890–904.
- [71] P. Yang, G. Ren, W. Liu, Spatial and Temporal Characteristics of Beijing Urban Heat Island Intensity, *J. Appl. Meteorol. Climatol.* 52 (8) (2013) 1803–1816.
- [72] A. Martilli, E.S. Krayenhoff, N. Nazarian, Is the Urban Heat Island Intensity Relevant for Heat Mitigation Studies? *Urban Clim.* 31 (2020), 100541.
- [73] T.R. Oke, The Energetic Basis of the Urban Heat Island, *Q. J. R. Meteorol. Soc.* 108 (455) (1982) 1–24.
- [74] P. Alexander, G. Mills, Local Climate Classification and Dublin’s Urban Heat Island, *Atmosphere* 5 (4) (2014) 755–774.